

Neural 3D decoding for human vision diagnosis

Li Zhang^{*1}, Yuankun Yang^{*1}, Ziyang Xie², Zhiyuan Yuan¹, Jianfeng Feng¹, Xiatian Zhu^{†3}, and Yu-Gang Jiang^{*1}

¹Fudan University

²University of Illinois at Urbana-Champaign

³University of Surrey

*Equal contribution

†Equal last authorship

<https://github.com/fudan-zvg/Brain3D>

ABSTRACT

Understanding the hidden mechanisms behind human's visual perception is a fundamental question in neuroscience. To that end, investigating into the neural responses of human mind activities, such as functional Magnetic Resonance Imaging (fMRI), has been a significant research vehicle. However, analyzing fMRI signals is challenging, costly, daunting, and demanding for professional training. Despite remarkable progress in artificial intelligence (AI) based fMRI analysis, existing solutions are limited and far away from being biologically meaningful and practically useful. In this context, we leap forward to demonstrate how AI can go beyond the current state of the art by advancing from 2D visuals to visually plausible and functionally more comprehensive 3D visuals decoded from brain signals, enabling automatic more sophisticated modeling of fMRI data. Innovatively, we reformulate the task of analyzing fMRI data as a *conditional 3D object generation* problem. We design a novel 3D object representation learning method, Brain3D, that takes as input the fMRI data of a subject who was presented with a 2D image, and yields as output the corresponding 3D object visuals. Importantly, we show that our AI agent captures the distinct functionalities of each region of human vision system as well as their intricate interplay relationships, aligning remarkably with the established discoveries of neuroscience. Non-expert diagnosis indicate that Brain3D can successfully identify the disordered brain regions in simulated scenarios, such as V1, V2, V3, V4, and the medial temporal lobe (MTL) within the human visual system. We also present results in cross-modal 3D visual generation setting, showcasing the perception quality of our 3D generation.

1 Introduction

Understanding how humans see and perceive the world is a fundamental question in neuroscience and vision^{1,2}. The ability to perceive and interpret the environment in three dimensions (3D) is a critical aspect of human vision that enables human to navigate, interact, and make sense of the world around us³⁻⁵. Despite significant advancements in the understanding of the neural mechanisms underlying visual perception⁶⁻⁹, the intrinsic processes involved in 3D vision remain largely unexplored.

Traditional approaches in neuroscience and life sciences, such as animal studies¹⁰⁻¹² and invasive techniques^{13,14}, have provided valuable insights but are limited by several factors. These limitations include the need for animal sacrifice¹⁵, ethical concerns^{16,17}, and interspecies heterogeneity¹⁸, which can hinder the translation of findings to human vision. Additionally, traditional methods often lack the spatial and temporal resolution necessary to capture the complex dynamics of neural activity underlying 3D vision perception. These limitations have restricted the progress of research in this field and highlight the need for novel interdisciplinary approaches.

Artificial vision, which aims to develop computational models inspired by biological vision¹⁹⁻²¹, has emerged as a promising avenue for understanding the neural basis of visual perception. While artificial vision models have achieved remarkable

success in various computer vision tasks, such as object recognition²²⁻²⁴, detection²⁵⁻²⁷, and scene understanding^{28,29}, their contribution to understanding biological vision remains limited. These models primarily focus on replicating human-like performance on specific tasks using visual input, without directly incorporating brain signals or mimicking the neural processes involved in biological vision. Furthermore, these models are not designed to simulate the effects of brain signal perturbations on vision, which is crucial for understanding vision-related brain regions.

Neural decoding models have focused on extracting essential representations of brain signals for visual content prediction³⁰⁻³³ and object recognition^{34,35}. These investigations have also shown promise in reconstructing images³⁶ from fMRI data using techniques such as generative adversarial networks^{37,38} and latent-space diffusion^{39,40}. However, these studies are currently limited to single views, which constrains their ability to model and analyze the underlying human brain's 3D visual processing capabilities.

To bridge this gap and gain deeper insights into how the human brain processes and interprets visual information, here we explore the intrinsic 3D human vision perception through the lens of fMRI data⁴¹, known for its high spatial resolution, relatively low cost compared to other neuroimaging techniques, and non-invasiveness. We introduce Brain3D, a bio-inspired

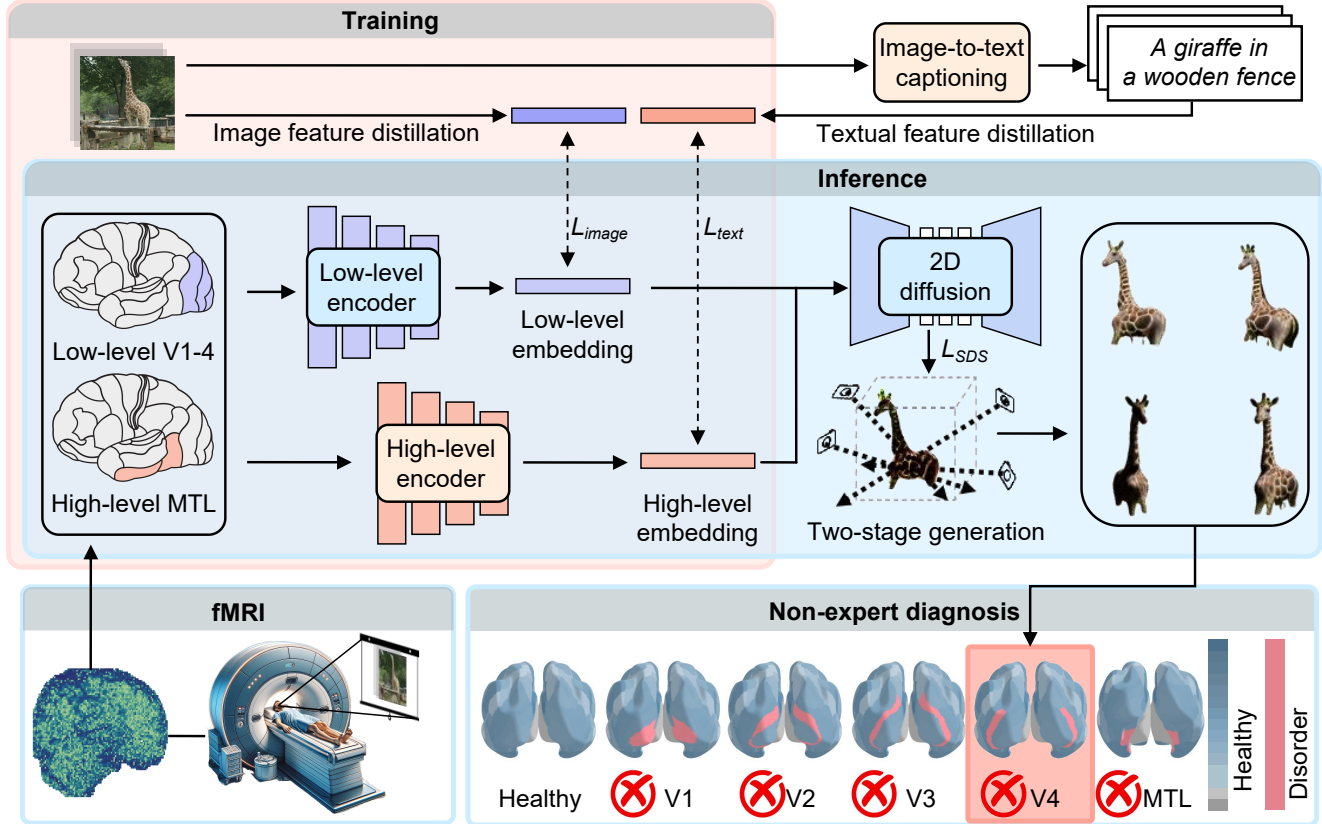


Figure 1. Brain3D: Processing brain fMRI for clinical diagnosis. The subject’s visual system first precepts the object stimulus, triggering specific patterns of activity in the brain’s visual processing areas which is then captured and expressed by fMRI data. Brain3D then leverages a fMRI encoder to extract the feature, feeds it into a 2D diffusion model for detailed 3D generation. The training procedure involves optimizing low-level and high-level encoders with the feature distillation objective L_{image} and L_{text} respectively, each incorporating bidirectional CLIP⁸⁶ contrastive learning and MixUp⁸⁵ augmentation for enhanced generalization. By contrasting the object stimulus and generated 3D visuals, even a non-expert can conduct precise diagnosis of atypical neurological conditions.

method capable of understanding how the brain interprets and processes visual stimuli in 3D. Brain3D takes fMRI data of a subject presented with a 2D object image and yields the corresponding 3D object model. Importantly, our AI agent captures the distinct functionalities and interplay relationships of each region in the human vision system, aligning with established neuroscience discoveries. This alignment allows Brain3D to serve as a powerful tool for clinical fMRI diagnosis, offering innovative diagnostic and therapeutic approaches in neurology and psychology. Preliminary experiments demonstrate that our AI agent can effectively diagnose regions associated with disorders, including V1, V2, V3, V4, and the medial temporal lobe (MTL). This research pioneers the understanding of the neural basis of human 3D vision with artificial neural networks, shedding light on cognitive processes and paving the way for theoretical exploration and practical applications in neuroscience.

2 Results

Overview of fMRI-based 3D scene synthesis by Brain3D. As a bio-inspired method our Brain3D can understand how the brain interprets and processes visual stimuli in 3D (Fig. 6). It efficiently maps 2D visual stimuli into 3D generations by analyzing the intricate functionalities of distinct brain regions.

Specifically, our model first deploys two specialized neural encoders to encode fMRI data into multi-level neural embeddings (Fig. 6a-d). The low-level encoder is designed to encode fMRI data from the basic visual cortex (V1 to V4), focusing on visual details such as color, shape, and texture, into low-level neural embeddings. Concurrently, the high-level encoder concentrates on the medial temporal lobe (MTL) to process visual information, such as object semantics and types. It encodes fMRI data from the MTL regions to high-level embeddings. Additionally, we introduce a UMAP-based projection⁷⁷ to further reduce noise in the high-level embeddings by decomposing these embeddings into separate distinct representations.

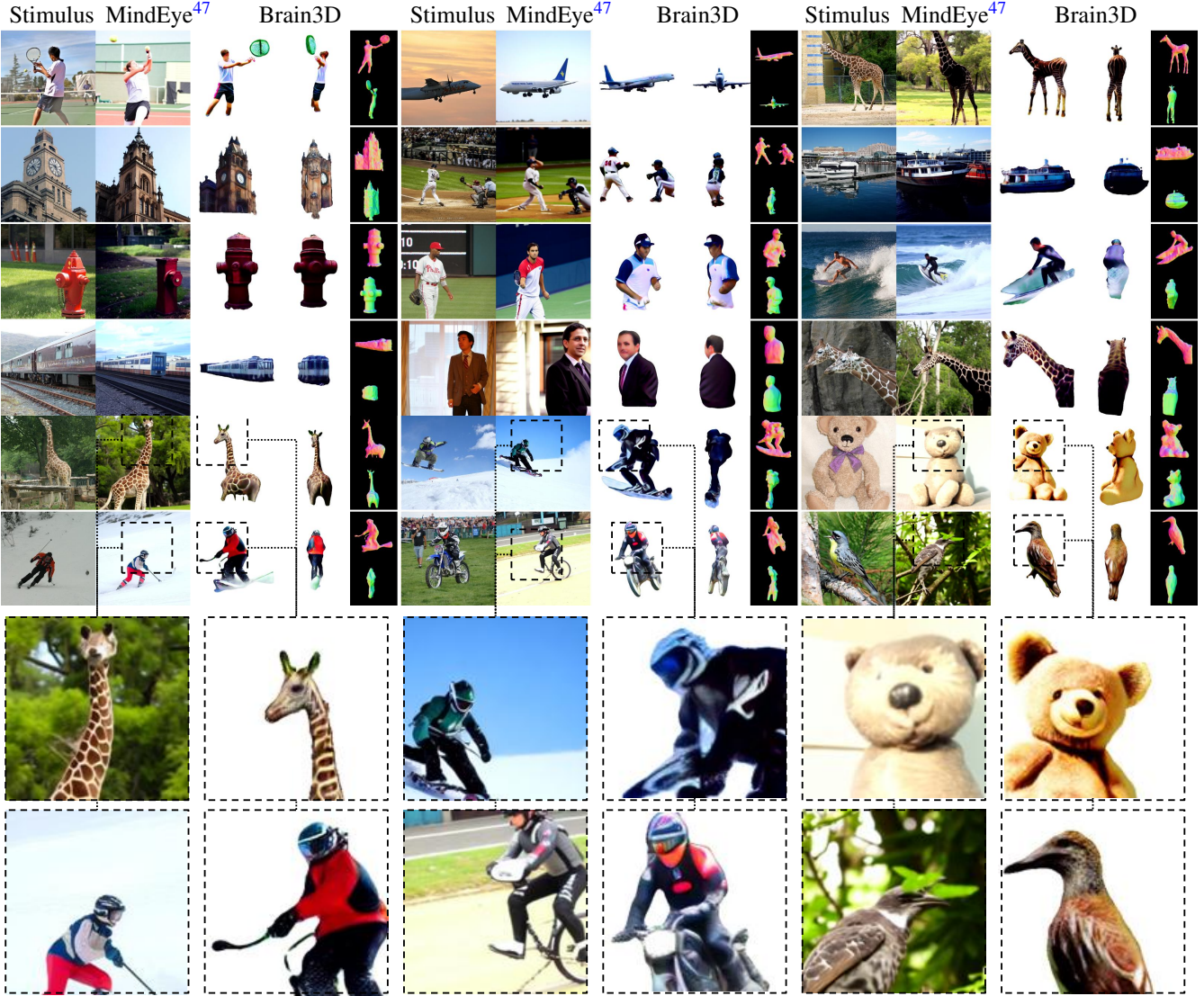


Figure 2. Brain3D generates finer 3D visuals from fMRI under 2D stimuli compared with previous methods. For each case, the first column displays the 2D stimuli presented to the subjects. The second column presents 2D reconstruction from MindEye⁴⁷. The three and fourth column exhibits two distinct views of our 3D visuals generated from fMRI, followed by the final column depicting the surface normals of our generation, yielding higher quality output than MindEye⁴⁷. The zoom-in visualizations in the last two rows demonstrates our better quality and more accurate fMRI-based generation.

Subsequently, we design a two-stage diffusion method⁴²⁻⁴⁴ to reconstruct the corresponding 3D objects. 3D objects are generated through distilling a 2D diffusion model with condition on both the high level and low level fMRI embeddings, using Score Distillation Sampling (SDS)⁴⁵ (Fig. 6f). For high-fidelity visual production, we employ a coarse-to-fine optimization strategy, with the Neural Radiance Field (NeRF)⁴⁶ as 3D scene representation for initial geometry learning followed by 3D mesh representation learning for detail recovery (Fig. 6e). The results affirm Brain3D’s effectiveness in modeling human vision process and diagnosing neurological abnormalities across multiple brain regions, including V1, V2, V3, V4, and the medial temporal lobe (MTL).

Demanding challenges with fMRI-based 3D generation. Generating 3D visual models from brain signals poses formidable challenges, especially concerning the collection and interpretation of fMRI signals. Recording brain responses from multiple angles simultaneously is technically demanding and costly, particularly in scenarios resembling real-world environments where only limited viewpoints are available. Additionally, the intricate distribution of brain regions further complicates the processing, resulting in a significant diversity of high-level information. Decoding and effectively utilizing this variety of information becomes exceedingly challenging, particularly when the amount of fMRI data is limited and costly to acquire. These challenges underscore the substantial

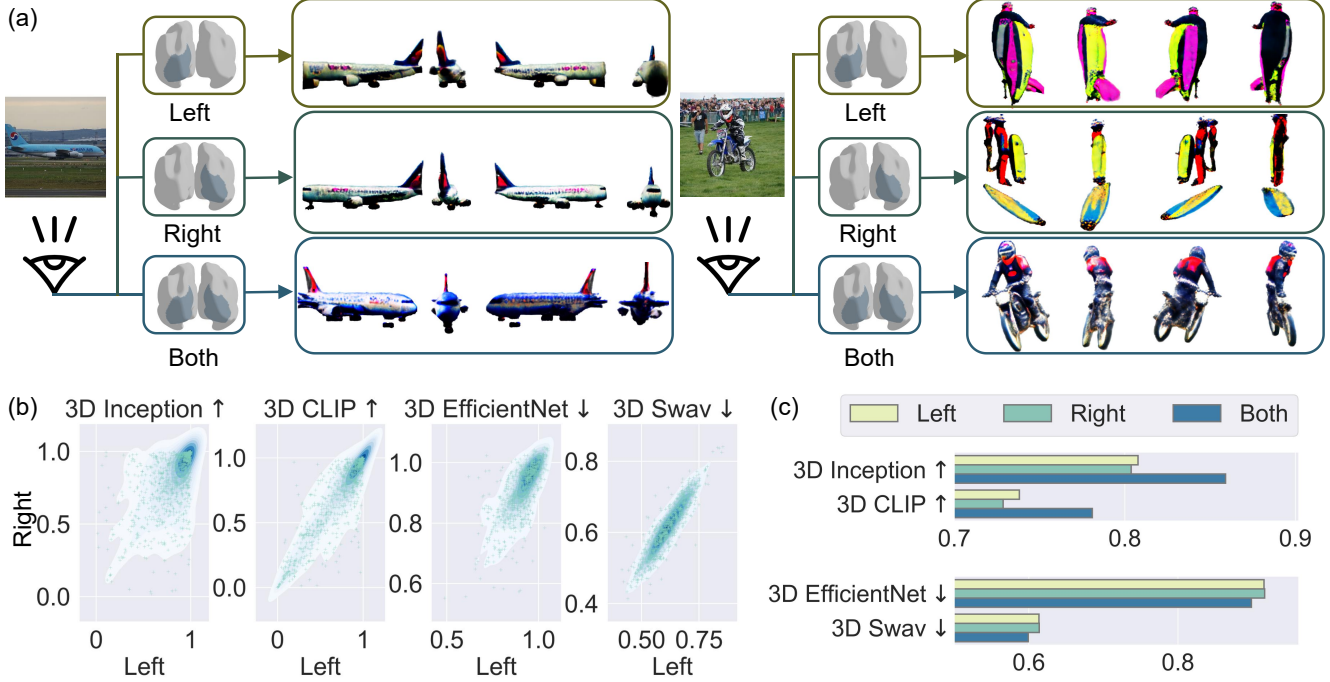


Figure 3. Collaborative property of the left and right hemispheres with Brain3D. (a) To examine the difference and interaction between the human brain’s two hemispheres, we conduct specialized experiments assessing 3D generation quality using fMRI from either hemisphere or both. (b) The function of the left and right hemispheres varies significantly for different specific objects under various metrics. In general, the left favors finer details and intricate structures, while the right focuses more on overall shape and silhouette. (c) Notably, using a combination of data from both hemispheres led to an enhanced generation. This synergistic effect was evident in improved performance across various metrics. More examples can be found in Fig. s7.

difficulties in advancing fMRI-based 3D modeling techniques within the field of neuroscience.

Brain3D decodes 3D models solely from fMRI signals with finer semantics in comparison to previous 2D models. To test the effectiveness of Brain3D in 3D generation, we perform comprehensive comparisons with an existing 2D method⁴⁷. We establish 3D-based evaluation benchmarks, including 3D Inception⁴⁸, 3D CLIP⁴⁹, 3D EfficientNet⁵⁰, and 3D Swav⁵¹, for subsequent evaluations (see Sec. 4.6 for detailed descriptions of these benchmarks). From the fMRI data Brain3D extracts rich appearance, semantic and geometric information, presenting a high degree of consistency with the stimuli images (Fig. 2). Despite limited observation with the giraffe, skier and teddy bear in the three cases (see the last two rows of Fig. 2), our bio-inspired model can process 3D details and comprehend their semantics beyond what is immediately visible in the 2D image, achieving finer semantic details than MindEye⁴⁷. This result underscores the remarkable human’s neural processing capability in constructing intricate 3D structures by interpreting and internalizing 3D geometric information from 2D visual stimuli⁵².

Enhanced visual quality through collaboration between the left and right hemispheres. We investigate whether

our model presents biological consistency in terms of regional functionalities. We first examine the roles of the left and right brain hemispheres, as well as their collaboration during the 3D object reconstruction process (Fig. 3a).

Specifically, we observe that the two hemispheres make different holistic contributions to object perception, due to exhibiting distinct performances for specific objects (Fig. 3b). The left hemisphere tends to depict finer details and intricate structures in object visualization, while the right hemisphere better captures the overall shape and silhouette. These results align with previous discoveries that the left hemisphere is involved in detail-oriented tasks while the right hemisphere in more holistic tasks^{53,56}. However, our results challenge the notion of strict functional division. We found notable overlaps and interactions between the two hemispheres. Remarkably, numerous objects rendered by the right hemisphere, as illustrated in Fig. 3a and Fig. s7, also exhibit intricate textures—typically a characteristic attributed to the left hemisphere. Conversely, the left hemisphere demonstrated capability in detecting overarching shapes, which is usually a strength of the right hemisphere.

Despite these different functional tendencies, our quantitative analysis, using metrics like 3D Inception, 3D CLIP, 3D EfficientNet, and 3D Swav in Fig. 3c, shows that both hemi-

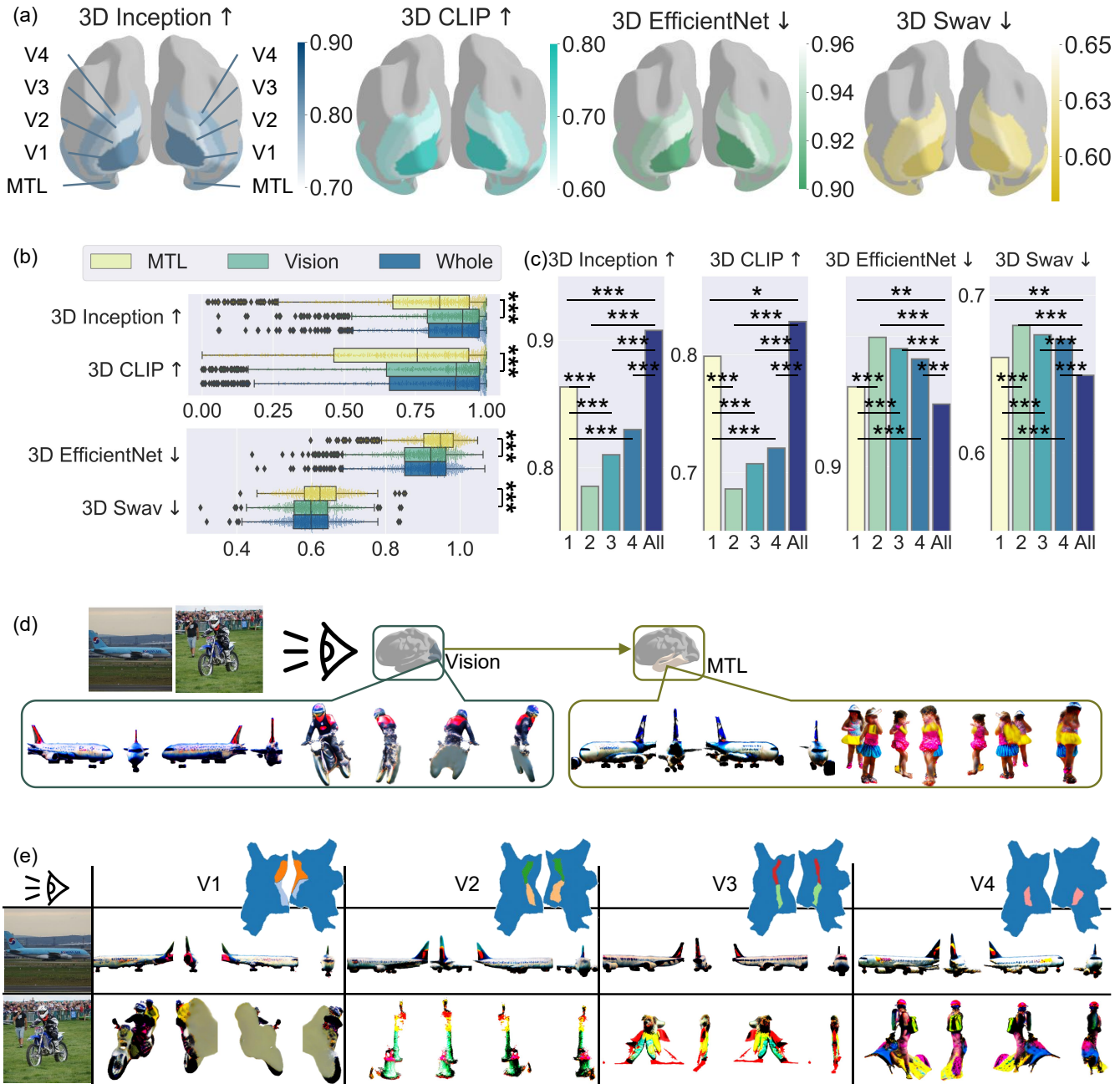


Figure 4. Visual region predominates in comprehension. (a) Overall, visual regions outperform the medial temporal lobe (MTL) regions under varying metrics. Further, V1 contributes the most among visual regions. (b) The vision region demonstrates a higher 3D generation quality with elevated performance. The significance level for MTL vs vision is: 3D Inception: $p=1e-23$, 3D CLIP: $p=1e-16$, 3D EfficientNet $p=1e-22$, 3D Swav $p=3e-15$. Performance of each generated object in these criteria is represented by crosses (+). (c) V1 Regions exhibit better performance than V2, V3 and V4 in generation. The significance level is: **3D Inception** V1 vs. (V2, V3, V4) $p=(1e-17, 4e-9, 9e-5)$, (V1, V2, V3, V4) vs. all $p=(3e-8, 1e-47, 4e-32, 6e-24)$. **3D CLIP** V1 vs. (V2, V3, V4) $p=(1e-30, 6e-23, 2e-18)$, (V1, V2, V3, V4) vs. all $p=(9e-3, 3e-31, 2e-23, 7e-19)$. **3D EfficientNet** V1 vs. (V2, V3, V4) $p=(6e-23, 1e-18, 7e-10)$, (V1, V2, V3, V4) vs. all $p=(5e-4, 1e-51, 1e-33, 2e-21)$. **3D Swav** V1 vs. (V2, V3, V4) $p=(2e-11, 2e-6, 1e-4)$, (V1, V2, V3, V4) vs. all $p=(1e-4, 4e-26, 5e-18, 8e-15)$. Significance levels are indicated as * = $p < 1e-2$, ** = $p < 1e-3$, *** = $p < 1e-4$. (d) MTL region tends to extract semantic visual concepts, while the visual cortex concentrates on textures and silhouettes. (e) V1 dominates in inferring the object silhouette, whilst V2, V3, and V4 are more focused on detailed aspects of texture. More examples can be found in Fig. 8.

spheres contribute similarly to 3D object perception. Their collaboration significantly contributes to the quality of 3D objects (Fig. 3c). This result echoes the biological discovery on the interaction between the left and right brain^{53–55}.

Dominance of V1 visual regions in feature and silhouette processing. We further investigate the functionalities of the various visual regions and the medial temporal lobe (MTL) region (Fig. 4a).

Previous studies have demonstrated that the visual cortex⁵⁷ is predominantly involved in processing color and texture information, whereas the medial temporal lobe (MTL) region^{58–60} is more focused on semantic information. In comparison, our research shows that the visual cortex exhibits higher visual decoding ability than MTL region (Fig. 4b). The significance level refers to the probability of error when rejecting the null hypothesis that visual cortex shares the similar performance as MTL region. Specifically, the visual cortex captures local fine-grained visual information such as the “windows” of an airplane and the “motorcycle rider”, while the MTL region captures holistic shapes like “airplane skeleton” and “person” (Fig. 4d). This visualization highlights higher-level 3D-shape-related concepts while foregoing pixel-level details. This finding provides a novel perspective on how the MTL region may contribute to the formation and recall of long-term memories, emphasizing its role in abstracting complex visual information.

In line with earlier researches^{6,7}, V1 region exhibits predominant ability in visual representation (Fig. 4c) among various visual regions. To further break down, V1 region plays a pivotal role in handling elementary visual information, including edges, features, and color. V2 and V3 regions play a role in synthesizing various features into complex visual forms, while V4 region focuses on basic color process at coarse level (Fig. 4e). However, our research brings to light a nuanced understanding of the interdependence within the visual cortex. Specifically, we demonstrate the reliance of the V2, V3, and V4 regions on the V1 region for constructing 3D vision. This is evident from the disrupted 3D geometries observed in Fig. 4e. This reliance likely stems from the fact that these regions process information initially received by V1¹, indicating a foundational dependence on V1 for effective visual processing. These findings emphasize the collaborative and interactive roles of these brain regions in forming a comprehensive visual representation. This result is thus biologically consistent to great extent.

Brain3D can diagnose regions with disorder. Motivated by the high biological consistency in terms of regional functions, we examine the usefulness of Brain3D in diagnosing disordered brain regions by designing a series of simulation based experiments (Fig. 5a). To compare performance of Brain3D and 2D models, we designed three branches of experiment: 2D model MindEye⁴⁷, Brain3D front view and Brain3D back view. In each branch, the participants were tasked with determining the impacted brain region of the pa-

tient from V1, V2, V3, V4, and MTL by observing 3D visuals generated from their fMRI signals. Their average correctness of judgement is represented as evaluation of clinical diagnosis. Notably, almost perfect diagnosis is achieved for the disorders with the V1 and MTL regions (Fig. 5b). However, distinguishing the disorders among V2, V3, and V4 regions presents more challenges, as reflected by the incidence of incorrect diagnoses in these areas. This difficulty is attributed to the significant overlap and interaction in their processing roles, as they all engage in visual information processing following the V1 region. Nonetheless, when a disorder was localized to a single region among V2, V3, or V4, participants generally succeeded in identifying that the issue stemmed from one of these three regions, despite the nuanced differences in their functionalities. Diagnosis among all regions in Brain3D outperforms previous 2D methods (Fig. 5c). We provide visual examples for region disorder diagnosis (Fig. 5d). V1 disorder tends to cause significant distortion to the output, consistent with the earlier finding about its critical role in processing basic visual information. Disorder in V2 region leads to changes in the detailed shape and motion of objects, e.g., orientation of the airplane and shape of the motorcycle. V3 region primarily affects the details and movements, e.g., the change from motorcycle to rider. Disorder in V4 region might cause color shift and variation. Instead, MTL’s disorder could be concerned with high-level semantics, e.g., increased ambiguity in object appearance. See Sec. 4.8 for more details.

Brain3D’s ability to generate 3D objects from fMRI data significantly contributes to this diagnostic efficiency. This capability is especially beneficial in assessing the MTL region. Without 3D information from the front view, disorders in the MTL region exhibit minimal impact, as the ‘Front’ column in Fig. s1c remains nearly unchanged. This is likely because the visual region still efficiently extracts the silhouette from the front perspective. However, the absence of high-level information due to a disordered MTL region leads to a much vaguer back view, creating a stark contrast to the normal state. The inclusion of this back view in diagnosis significantly improves accuracy, as demonstrated in Fig. s1a with a limited number of images. The use of the back view in diagnostic assessments also enhances the accuracy of diagnoses across all visualizations from patients, as shown in Fig. s1b. This improved diagnostic capability might stem from the impaired MTL region’s reduced ability to use semantic information for understanding unseen perspectives in a given 2D image. In 2D model⁴⁷, although abnormalities in the MTL brain area also lead to changes in the generated 2D images (Fig. s1c), these changes do not have obvious features, making it difficult to distinguish and diagnose from other brain area abnormalities (such as V1 abnormalities). This directly leads to a significant decrease in the success rate of diagnosing the MTL brain region (Fig. s1a). In comparison, Brain3D reasonably exploits MTL region, thus being able to distinguish disorders in MTL from other brain regions more directly by the blurring in the back view (Fig. s1c). This demonstrates that the 3D visual-

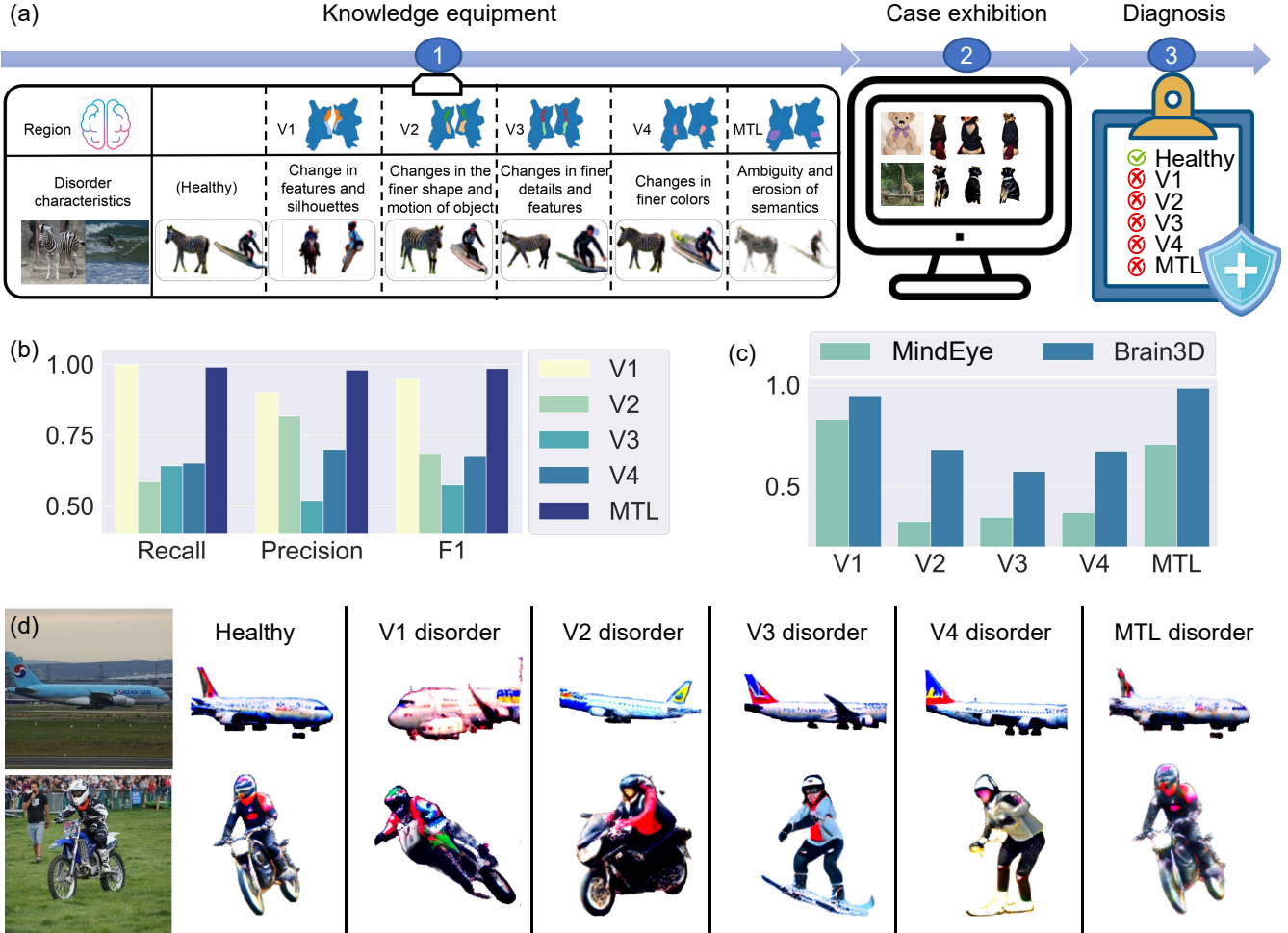


Figure 5. Illustration of Brain3D to process fMRI for clinical diagnosis. (a) In non-expert diagnosis, participants are first equipped with knowledge about the function with varying visual system regions (V1, V2, V3, V4, MTL) and a number of case study for their diagnosis practice. We show cases both with and without disorders for information. (b) Regional disorder diagnosis performance by non-professionals using our Brain3D. (c) 3D representation of Brain3D achieves improved F1 diagnosis score than 2D model. (d) Visual example of disorder diagnosis with Brain3D.

ization capabilities of Brain3D are vital for clinical diagnosis and comprehending 3D human vision.

To explore more cost-effective diagnostic methods, our study extended to experiments where participants were provided with a limited number of visualizations for brain disorder diagnosis. This approach was driven by the desire to ascertain if accurate diagnostics could be attained with fewer resources such as time and cost. The results were significant, as demonstrated in Fig. s2: even with a reduced number of images, participants were able to accurately tell disorders in the V1 and MTL regions, significantly cutting down the time and resources usually needed for thorough diagnoses. Specifically, even with as few as 10 images (Fig. s2a), participants achieved over 95% of diagnostic accuracy for disorders in the V1 and MTL regions. This implies that by utilizing merely 10% of the potential images from patients, we can still reach a plausible diagnosis of V1 and MTL region thereby saving almost

90% of the time and effort as required in our full diagnostic process.

Ablation analysis. Our perceptual pipeline employs Score Distillation Sampling (SDS)⁴⁵ with the inclusion of both low-level and high-level guidance. The integration of both low-level and high-level guidance achieves the best performance across all categories (Fig. s3a). As shown in Fig. s3b, when solely relying on high-level guidance, the representations of the train, airplane, and clock tower appear significantly blurred, displaying only coarse shapes. These coarse shapes stem from the geometric and semantic information embedded within the high-level representation. Low-level guidance primarily captures the color and texture attributes of the objects. Consequently, the outcomes with low-level guidance (see the first column), featuring the front view, align well with the provided image, while other views fall short in terms of shape and semantic fidelity. The combination of both high-level and

low-level guidance results in significantly improved representations of the airplane, train, and clock tower, where both the semantic and textural structures closely resemble those of the testing image.

The Semantic Stage within our framework is designed to extract finer details from fMRI embeddings, enhancing its contribution to 3D generation. After the Semantic Stage the detailed textures of the building in the first row and the outline of the steamship in the second row in Fig. s4c exhibit much greater clarity. These details from fMRI are challenging to represent in a coarse NeRF but can be effectively distilled within a 3D mesh.

The left four-column section in Fig. s5c and Fig. s10 displays the results obtained using high-level embeddings directly extracted from fMRI without the application of UMAP projection. In this scenario, the target distribution $p_\phi(\mathbf{z}_t|\mathbf{y}) = \int p_\phi(\mathbf{z}_t|c, \mathbf{y})p(c)dc$ is optimized with respect to \mathbf{y} . The multi-view integration $\int p_\phi(\mathbf{z}_t|c, \mathbf{y})p(c)dc$ integrates \mathbf{y} with high diversity and substantial noise, resulting in oversaturated and inconsistent generation outcomes. Following the incorporation of our designed UMAP projection, illustrated in the right four-column section in Fig. s5c and Fig. s10, the high-level information \mathbf{y} undergoes the transformation into a series of stable and consistent embeddings \mathbf{y}_i . Consequently, the target distribution is updated as $p_\phi(\mathbf{z}_t|\mathbf{y}_i) = \int p_\phi(\mathbf{z}_t|c, \mathbf{y}_i)p(c)dc$. This adjustment steers the 3D optimization process toward a more stable and consistent direction in each iteration. Despite setting different guidance \mathbf{y}_i sampled from the projection weight in each denoising iteration, the stability of the denoising step effectively ensures the attainment of a final stable generation.

3 Discussion

Understanding how human vision system extracts and processes the physical world is a critical question in neuroscience. For the first time, this research models the underlying mechanisms of human visual perception by mapping fMRI of human brain activities to the corresponding 3D objects. This goes beyond previous studies that are limited to statistical fMRI analysis^{1,2,7,54}.

Despite the advancements in our 3D generation and clinical diagnosis, discrepancy remains between the generated objects and the actual images viewed by participants. This phenomenon can be attributed in part to cognitive biases⁹² and the inherent blurring effects⁹³ that occur during the image-to-fMRI cognitive stage. An example of this can be seen in the last row of Fig. 2 where the bird's beak appears shut. This is because the upper half of the beak appears similar as the background, illustrating how visual processing and brain interpretation can influence our visual perception. Signal resolution also plays a significant role. The 1.8 mm resolution of fMRI data leads to a loss of fine details, particularly in smaller neuronal structures. In addition, current 3D generation models also struggle to accurately capture background details that extend beyond the camera's field of view. These

limitations highlight the challenges in accurately representing and analyzing complex visual information.

By enabling deeper and more direct analysis of visual perception, our study opens up a more advanced and convenient approach to the clinical diagnosis of brain disorders. Previous fMRI-based diagnostic techniques primarily focused on detecting variations in signal frequency within specific brain regions, such as the motor area for Parkinson's disease^{61,62}, the premotor and motor cortices in cases of Dystonia⁶³⁻⁶⁵, and motor networks for tremor^{66,67} and Huntington's disease⁶⁸⁻⁷⁰. However, such methods, relying solely on activation frequency, can be limited due to their narrow focus on direct statistical analysis of fMRI signals, which may not fully account for the variability inherent in fMRI, particularly in the context of disorders. For instance, Parkinson's disease may exhibit both decreased^{71,72} and increased^{73,74} in the motor area, while Dystonia also shows conflicting fMRI activity levels⁶³⁻⁶⁵. In contrast, Brain3D represents a more sophisticated and intuitive diagnostic approach by attempting to recover the target objects from fMRI. The key is our capacity in encoding the functionality of various brain regions that can be easily visualized in the output. As a result, the clinical diagnose process is made significantly simpler and efficient.

Our research also highlights the human brain's remarkable capability in perceiving 3D-related high-level information from 2D visual stimuli. This perception is facilitated by the synergistic functions of both brain hemispheres and the intrinsic collaboration between different functional regions. For example, the V1 region is fundamentally pivotal along with V2, V3, and V4 regions enhancing the perception through detail and color information, whilst the MTL region focuses on higher-level semantics. For the first time, we have attempted to simulate this intricate mechanisms of human visual perception by innovating a machine learning approach with great potentials for real-world applications.

4 Method

4.1 Pipeline overview

We aim to model the intricate mechanisms behind human vision perception. To achieve this, we develop Brain3D, a model capable of creating 3D representations from the fMRI signal of individual's minds. Given the fMRI signal collected during an individual viewing a 2D image, we decompose it into two parts according to the sources: visual cortex and MTL (Fig. 6a). The visual cortex focuses on the low-level texture feature, while the MTL captures the high-level semantics information. For each source, we design a specialized feature embedding encoder (Fig. 6b).

Formally, this process begins with an fMRI voxel \mathbf{X}_i . We employ encoders to transform \mathbf{X}_i into two types of embeddings: a low-level embedding $f_L(\mathbf{X}_i)$, and a high-level embedding $f_H(\mathbf{X}_i)$ (Fig. 6c). These embeddings are then supervised by respective features under image and textural feature distillation (Fig. 6d). This multi-level structure thus separates the high-level semantics information and the low-level texture de-

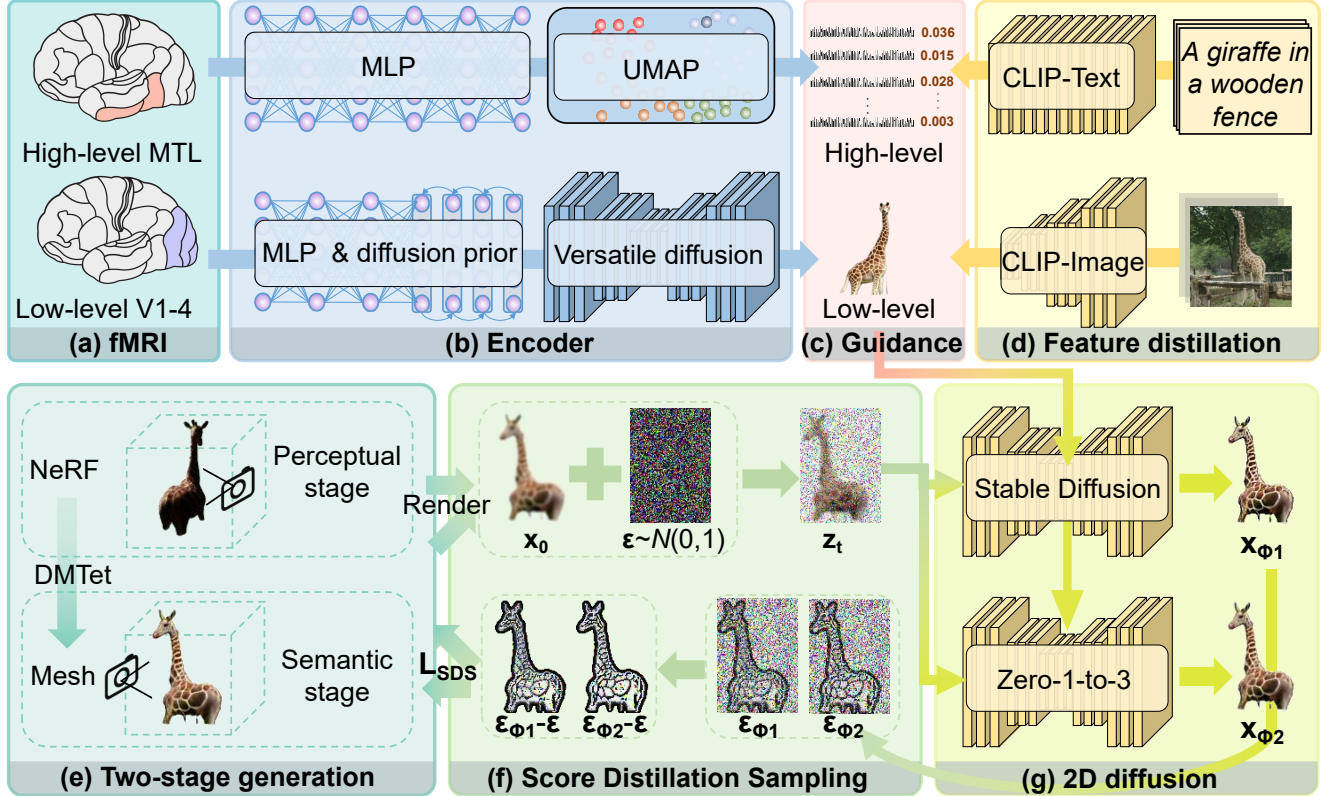


Figure 6. Overview of our Brain3D that decodes the functional MRI (fMRI) signals into 3D reconstructions. (a)

Initially, the subject's visual system precepts the object stimulus, which triggers specific patterns of neural activity within the brain's visual processing areas. These patterns are recorded as fMRI signals. (b) To generate the 3D object, Brain3D employs two specialized encoders: the high-level encoder uses MLP and UMAP⁷⁷ to capture abstract, high-level visual concepts, while the low-level encoder processes basic visual details via Versatile diffusion⁸¹. (c) Both encoders process fMRI to extract respective information for representing 3D objects. (d) These encoders are optimized through feature distillation, which utilize pretrained CLIP-Text and CLIP-Image encoders⁸⁶ as the guidance for the high-level and low-level features, respectively. (e) The 3D object generation process includes two phases: the perceptual phase utilizes NeRF⁴⁶, and the semantic phase transforms NeRF output into a 3D mesh⁸³ using DMTet⁸². (f) The 3D object is refined using Score Distillation Sampling (SDS)⁴⁵, which introduces Gaussian noise into a randomly-viewed rendered image and employs 2D diffusion models for noise prediction. (g) The high-level and low-level feature guidance both are served as conditions for the pretrained Stable Diffusion⁴³ and Zero-1-to-3⁷⁹ models to predict the added noise.

tails of the fMRI signal, simulating the biological information processing^{75,76}. The final 3D objects are reconstructed using a two-stage generative diffusion pipeline conditioned on both the low-level and high-level fMRI embeddings(Fig. 6e).

4.2 Preliminary: Diffusion based 3D generation

Our approach employs a diffusion model⁴² aimed at manipulating data through a two-phased process. Initially, a forward process introduces Gaussian noise with parameter (α_t, σ_t) into the data \mathbf{x}_0 to achieve noised input \mathbf{z}_t , which can be mathematically represented as follows:

$$q_t(\mathbf{z}_t|\mathbf{x}_0) = N(\alpha_t \mathbf{x}_0, \sigma_t^2 I) = \int q_t(\mathbf{z}_t|\mathbf{x}_0) q_0(\mathbf{x}_0) d\mathbf{x}_0. \quad (1)$$

Following this, a reverse process is employed to denoise the data, starting from pure noise. This reverse mechanism is

driven by a parameterized noise prediction network $\epsilon_\phi(\mathbf{x}_t, t)$, optimized by minimizing the objective loss function as:

$$L_{\text{Diff}}(\phi, \mathbf{x}) = \mathbb{E}_{t \sim U(0,1), \epsilon \sim N(0,1)} [\omega(t) |\epsilon_\phi(\alpha_t \mathbf{x} + \sigma_t \epsilon, t) - \epsilon|_2^2]. \quad (2)$$

This mechanism is further extended to 3D generation through the integration of Score Distillation Sampling (SDS)⁴⁵ (Fig. 6f). It involves two key components: a scene model and a pre-trained Text-to-Image (T2I) diffusion model. The scene model, parameterized by θ , generates differentiable images through $\mathbf{X}_i = g(\theta)$. The pre-trained T2I diffusion model predicts the sampled noise $\epsilon_\phi(\mathbf{X}_i, t, \mathbf{y})$ conditioned on the noisy image \mathbf{X}_i , created by adding Gaussian noise with a random scale factor t to \mathbf{X}_i . The optimization of this extended

model is guided by the following objective:

$$\begin{aligned}\nabla_{\theta} \mathcal{L}_{SDS}(\phi, \mathbf{X}_i) &= \mathbb{E}_{t, \varepsilon}[\omega(t)(\hat{\varepsilon}_{\phi}(\mathbf{X}_{it}; t, \mathbf{y}) - \varepsilon_t) \frac{\partial \mathbf{X}_i}{\partial \theta}] \\ &= E_{t, \mathbf{z}_t} | \mathbf{X}_i | [\omega(t) \frac{\sigma_t}{\alpha_t} \nabla_{\theta} KL(q(\mathbf{z}_t | \mathbf{X}_i = g(\theta)) || p_{\phi}(\mathbf{z}_t | \mathbf{y}))].\end{aligned}\quad (3)$$

Through this computation, our model seeks to align the generated distribution $q(\mathbf{z}_t | \mathbf{X}_i = g(\theta))$ closely with the target distribution $p_{\phi}(\mathbf{z}_t | \mathbf{y})$, ensuring consistency across various camera poses, as detailed in the following integration:

$$p_{\phi}(\mathbf{z}_t | \mathbf{y}) = \int p_{\phi}(\mathbf{z}_t | c, \mathbf{y}) p(c) dc. \quad (4)$$

This integration necessitates consistency in $p_{\phi}(\mathbf{z}_t | c, \mathbf{y})$ from each camera pose c .

4.3 Tackling high noises with high-level semantics

In modeling human mind signals, a major challenge arises from the intrinsically significant levels of noise and diversity with the high-level information within the human brain (Fig. 6). This can cause instability in the conditional probability distribution $p_{\phi}(\mathbf{z}_t | c, \mathbf{y})$ (see Sec. 4.2 for more details), particularly when considering different camera angles, denoted as c . This instability could result in a lack of consistency for 3D object generation. Addressing this issue is critical for ensuring that our model reliably interprets and reconstructs the complex fMRI scans.

We develop a novel approach to solving the above problem using the Uniform Manifold Approximation and Projection (UMAP)⁷⁷ (Fig. 6b). The key idea is to distill the high-level semantic embeddings into a series of representative embedding vectors with a unique projection weight.

Formally, following the transformation of fMRI \mathbf{X}_i into a high-level embedding by the MLP backbone f_H , this embedding $f_H(\mathbf{X}_i)$ is subsequently projected

into a set of stable embeddings, $\{f_{H_1}(\mathbf{X}_i), f_{H_2}(\mathbf{X}_i), \dots, f_{H_n}(\mathbf{X}_i)\}$, derived from the Generative Text-to-Image Transformer⁷⁸.

In our design, we concatenate the embeddings extracted from all training images. This results in a comprehensive set of embeddings, $\{f_H(\mathbf{X}_i), f_{H_1}(\mathbf{X}_i), f_{H_2}(\mathbf{X}_i), \dots, f_{H_n}(\mathbf{X}_i)\}$, for each image. These combined embeddings form a high-dimensional dataset, denoted as \mathbf{D} .

Then, we optimize the stable representation of these embeddings, with the goal to minimize the cross-entropy between the high-dimensional probability distributions and their corresponding stable embeddings. It is conducted via stochastic gradient descent for handling the complexity of such high-dimensional data.

For fMRI inference \mathbf{X}_i , we implement a pre-trained UMAP model, g_U , to project the high-level embeddings $\{f_H(\mathbf{X}_i), f_{H_1}(\mathbf{X}_i), f_{H_2}(\mathbf{X}_i), \dots, f_{H_n}(\mathbf{X}_i)\}$ into a stable space. The resultant embeddings are represented as $\{\mathbf{U}_H, \mathbf{U}_{H_1}, \mathbf{U}_{H_2}, \dots, \mathbf{U}_{H_n}\}$ with each obtained as:

$$\mathbf{U}_{H_j} = g_U(f_{H_j}(\mathbf{X}_i)). \quad (5)$$

To quantify the similarity between \mathbf{U}_H and each \mathbf{U}_{H_j} , we calculate the cosine similarity, s_i , as follows:

$$s_i = \frac{\mathbf{U}_H \cdot \mathbf{U}_{H_j}}{|\mathbf{U}_H| \cdot |\mathbf{U}_{H_j}|}, \quad (6)$$

This similarity measurement is then normalized to establish a sampling probability for each embedding:

$$v_j = \frac{s_j}{|\mathbf{U}_{H_j}|}, \quad (7)$$

$$w_j = \frac{v_j}{\sum_{j=1}^n v_j}, \quad (8)$$

This normalization process is critical as it determines how embeddings are sampled during the denoising step of the 2D diffusion model. Under specific conditions, the linear space formed by $\{\mathbf{U}_{H_1}, \mathbf{U}_{H_2}, \dots, \mathbf{U}_{H_n}\}$ can effectively represent \mathbf{U}_H linearly, as described in the follows:

$$\mathbf{U}_H = \sum_{j=1}^n \text{proj}_{\mathbf{U}_{H_j}}(\mathbf{U}_H) = \sum_{j=1}^n \frac{\mathbf{U}_{H_j} \cdot \mathbf{U}_H}{|\mathbf{U}_{H_j}|^2} \mathbf{U}_{H_j} = |\mathbf{U}_H| \sum_{j=1}^n t_j \cdot \mathbf{U}_{H_j}. \quad (9)$$

In essence, the UMAP projection serves as a non-linear expression of the high-level embedding $f_H(\mathbf{X}_i)$, contributing significantly to our model's ability to handle complex data representations.

In diffusion model's inference step, we sample the projected embedding $f_{H_j}(\mathbf{X}_i)$ with probability w_j for denoising. This approach ensures a stable $p_{\phi}(\mathbf{z}_t | \mathbf{y}_i) = \int p_{\phi}(\mathbf{z}_t | c, \mathbf{y}_i) p(c) dc$. Consequently, the gradients of the loss function $\mathcal{L}_{SDS}(\phi, \mathbf{X}_i)$ are modified as follows:

$$\begin{aligned}\nabla_{\theta} \mathcal{L}_{SDS}(\phi, \mathbf{X}_i) &= \mathbb{E}_{t, i, \varepsilon}[\omega(t)(\hat{\varepsilon}_{\phi}(\mathbf{X}_{it}; t, \mathbf{y}_i) - \varepsilon_t) \frac{\partial \mathbf{X}_i}{\partial \theta}] \\ &= E_{t, i, \mathbf{z}_t} | \mathbf{X}_i | [\omega(t) \frac{\sigma_t}{\alpha_t} \nabla_{\theta} KL(q(\mathbf{z}_t | \mathbf{X}_i = g(\theta)) || p_{\phi}(\mathbf{z}_t | \mathbf{y}_i))],\end{aligned}\quad (10)$$

Here, the expectation of the sampled embedding i is integrated into the computation. This means we selectively utilize these weights to pick the most relevant high-level embeddings. This integration is crucial for ensuring that our model accurately captures and reconstructs the complex patterns inherent in fMRI data, producing more reliable and consistent multi-view visual results.

4.4 Two-stage 3D generation

To effectively leverage the projected high-level embeddings, we devise a two-stage 3D generation architecture characterized by progressively integrating high-level information during 3D object modeling (Fig. 6e). The first stage is a perceptual stage, utilizing the Neural Radiance Fields (NeRF)⁴⁶ for 3D representation. It defines an implicit 3D representation framework expressed as:

$$C(\mathbf{r}) = \int_{t_n}^{t_f} T(t) \sigma(\mathbf{r}(t)) \mathbf{c}(\mathbf{r}(t), \mathbf{d}) dt, \quad (11)$$

$$T(t) = \exp(-\int_{t_0}^t \sigma(\mathbf{r}(s))ds). \quad (12)$$

This framework allows the gradients from the Score Distillation Sampling (SDS)⁴⁵ to directly influence the output $C(\mathbf{r})$, enabling simultaneous optimization of the density Multilayer Perceptron (MLP) $\sigma(\mathbf{r}(t))$ and color MLP $(\mathbf{r}(t), \mathbf{d})$. As a result, NeRF is particularly effective at modifying both the color and shape of the 3D object in this stage. In our implementation, we incorporate Zero-1-to-3⁷⁹ for low-level guidance and Stable Diffusion⁴³ for high-level guidance.

Subsequently, a semantic stage follows where we employ DMTet⁸² to convert the above NeRF into a 3D mesh⁸³. This conversion prepares the 3D model for further processing. We continue to harness Stable Diffusion⁴³, coupled with a depth-conditioned Control-Net⁸⁴ for high-level guidance. While the 3D mesh does not possess the same versatility as NeRF in shaping modifications, it excels in capturing detailed RGB color information. Therefore, after establishing the coarse shape in the perceptual stage, we shift our focus to refining the color details in this stage. This two-tier design allows for an intricate and nuanced development of the 3D object, leading to a final output that is both elaborately detailed and of high resolution.

4.5 Training and inference

During training, we optimize the parameters for both low-level encoder and high-level encoder, leaving all the rest components frozen. The high-level encoder is detailed in Sec. 4.3, while the low-level encoder comprises MLP backbone, diffusion prior⁸⁰, and Versatile diffusion⁸¹. We use a training dataset with image-text pairs. Inspired by MindEye⁴⁷, the loss function for low-level L_{image} and high-level L_{text} embeddings are designed with integration of bidirectional CLIP⁸⁶ contrastive learning and MixUp⁸⁵ augmentation to improve generalization in the beginning of training stage, as described in the follows:

$$\begin{aligned} \mathcal{L}_{mix} = & - \sum_{i=1}^N [\lambda_i \cdot \log\left(\frac{\exp(\frac{p_i^* \cdot t_m}{\tau})}{\sum_{m=1}^N \exp(\frac{p_i^* \cdot t_m}{\tau})}\right) \\ & + (1 - \lambda_i) \cdot \log\left(\frac{\exp(\frac{p_i^* \cdot t_k}{\tau})}{\sum_{m=1}^N \exp(\frac{p_i^* \cdot t_m}{\tau})}\right)] \\ & - \sum_{j=1}^N [\lambda_j \cdot \log\left(\frac{\exp(\frac{p_j^* \cdot t_j}{\tau})}{\sum_{m=1}^N \exp(\frac{p_m^* \cdot t_j}{\tau})}\right) \\ & + \sum_{\{l|k_l=j\}} (1 - \lambda_l) \cdot \log\left(\frac{\exp(\frac{p_l^* \cdot t_j}{\tau})}{\sum_{m=1}^N \exp(\frac{p_m^* \cdot t_j}{\tau})}\right)], \end{aligned} \quad (13)$$

where τ represents the temperature hyperparameter, λ denotes the voxel-mixing coefficient obtained from a Beta distribution where $\alpha = \beta = 0.15$, and N is the batch size. The CLIP embedding t_i of a ground-truth image or text, denoted as y_i , is obtained as:

$$t_i = \text{CLIP}_{\text{image/text}}(y_i). \quad (14)$$

The p_i^* in Eq. (13) represents a fMRI embedding derived from either a low-level encoder f_L or a high-level encoder f_H , denoted as $f_{L/H}$, using the initial fMRI X_i . This process is obtained with MixUp augmentation⁸⁵ as the subsequent equations:

$$X_{\text{mix}_{i,k_i}} = \lambda_i \cdot X_i + (1 - \lambda_i) \cdot X_{k_i}, \quad (15)$$

$$p_i^* = f_{L/H}(X_{\text{mix}_{i,k_i}}), \quad (16)$$

After one third of the training stage, the BiMixCo loss for both L_{image} and L_{text} is replaced with soft contrastive loss to facilitate softmax probability distribution for improved knowledge distillation⁸⁷, expressed as:

$$\mathcal{L}_{soft} = - \sum_{i=1}^N \sum_{j=1}^N \left[\frac{\exp(\frac{t_i \cdot t_j}{\tau})}{\sum_{m=1}^N \exp(\frac{t_i \cdot t_m}{\tau})} \cdot \log\left(\frac{\exp(\frac{p_i \cdot t_j}{\tau})}{\sum_{m=1}^N \exp(\frac{p_i \cdot t_m}{\tau})}\right) \right]. \quad (17)$$

where the p_i represents fMRI embeddings derived from either low-level or high-level encoder $f_{L/H}$ through the following equation:

$$p_i = f_{L/H}(X_i). \quad (18)$$

During **inference**, we exclusively use pre-trained weights for fMRI extraction $p_i = f_{L/H}(X_i)$ and the subsequent 3D generation, relying entirely on fMRI data. This approach ensures that the model's inference is based purely on its understanding of fMRI data, without requiring any information such as the viewed image, nor external texts.

4.6 3D generation evaluation

To analyze the generation quality, we introduce four fMRI-to-3D evaluation metrics: 3D Inception⁴⁸, 3D CLIP⁴⁹, 3D EfficientNet⁵⁰, and 3D Swav⁵¹. These metrics are designed to overcome the limitations of traditional pixel-by-pixel image reconstruction metrics like PixelCorrelation⁹⁰, which lacks robustness against rotations and translations in 3D space. For comprehensive evaluation, we construct a level-2 icosahedron with a 2.2 radius around the generated 3D object and capture the 3D object from all the icosahedron vertices to achieve multi-view coverage, similar to the approach in the text-to-3D benchmark⁹¹. The metrics 3D Inception and 3D CLIP, utilizing the final pooling layer of InceptionV3⁴⁸ and CLIP model⁴⁹ respectively, assess the accuracy of two-way identification between original image embeddings and corresponding brain embeddings. Consequently, larger 3D Inception and 3D CLIP represent higher matching accuracy in features between ground truth images and generated 3D objects, indicating a well extracted features from fMRI. On the other hand, 3D EfficientNet and 3D Swav employ EfficientNet-B1⁵⁰ and SwAV-ResNet50⁵¹ to calculate the average correlation distance between the extracted features. Lower correlation distance represents higher correlation between ground truth images and generated 3D objects, representing better reconstruction. In order to address view inconsistency in the final quality evaluation, we implement a regional convolution mechanism to smooth the scores across the local region, which

treats the icosahedron as a graph composed of vertices and edges and performs mean pooling on this graph, employing a recursive formula:

$$s_i^{(t+1)} = \frac{1}{|N(i)|+1} (s_i^{(t)} + \sum_{j \in N(i)} s_j^{(t)}). \quad (19)$$

The highest score among all viewpoints is then selected as the ultimate quality score for the 3D generation.

4.7 Dataset

We conduct extensive experiments on the Natural Scenes Dataset (NSD)⁴¹. This dataset is comprised of high-resolution whole-brain fMRI measurements (1.8-mm isotropic resolution, 1.6-s sampling rate) from eight healthy adult subjects. These subjects were observed while viewing thousands of 2D colored natural images sampled from COCO dataset⁸⁸, spread across 30 to 40 scanning sessions. The two-stage training set includes 8,859 images and 24,980 fMRI trials, whereas the test set contains 982 images and 2,770 fMRI trials. To enhance data quality, we compute average fMRI responses for images that are presented more than once.

The fMRI signals are preprocessed and split into two specialized regions using predefined masks: the NSD General Region-of-Interest (ROI) mask and the Medial Temporal Lobe (MTL) mask, both at a resolution of 1.8 mm. The NSD General ROI mask encompasses regions such as V1, V2, V3, and V4, presenting a spectrum from the early visual cortex to higher visual areas, with an emphasis on low-level information. In contrast, the MTL mask encompasses brain regions including the hippocampus, amygdala, and parahippocampal regions, which are more attuned to high-level information.

4.8 Brain disorder diagnosis

Our model has the ability to translate complex fMRI signals into easily understandable multi-view object images. This empowers individuals, regardless of their professional background, to undertake disorder diagnosis with minimal training through a straightforward tutorial. This substantially lowers the barrier to entry for this task.

To simulate the disorders of varying brain regions, we adopt the general fMRI simulation techniques⁸⁹ that introduce Gaussian noises. We randomly select samples from the NSD test set for disorder simulation. For each sample, we apply independent Gaussian noises with a variance of 3.0 over five brain regions: V1, V2, V3, V4, and MTL, respectively.

In our diagnosis tutorial we show a participant several examples including the original image presented to a patient, and our model's output under the healthy situation and regional disorder in V1, V2, V3, V4, and MTL, along with a textural description of each disorder's characteristics. This tutorial can be easily conducted before the user study.

In our experiment, we invite 100 volunteer participants, each educated simply by the above tutorial. None of them possessed prior expertise in neuroscience or brain disorder diagnosis with fMRI. The diagnosis task is to detect which

brain region has disorder by comparing the original image and the generated images by our model. For diagnosing a specific patient, we use a various number {1, 5, 10, 20, 50, 100} of images and fMRI pairs associated. We evaluate the diagnosis performance by the metrics of precision, recall, and F1 score.

5 Data Availability

Our research utilize the publicly available Natural Scenes Dataset (NSD)⁴¹, which can be accessed freely for research and validation.

6 Code Availability

We enclosed our code and training steps in submission. Our github repository is <https://github.com/fudan-zvg/Brain3D>. Supplementary materials with video visualizations of more 3D generations are available at <https://brain-3d.github.io/>.

References

1. Hubel, D. H., Wiesel, T. N. Brain mechanisms of vision. *Scientific American*, 241(3), 150-163. (1979).
2. Hupé, J. M., James, A. C., Payne, B. R., Lomber, S. G., Girard, P., Bullier, J. Cortical feedback improves discrimination between figure and background by V1, V2 and V3 neurons. *Nature*, 394(6695), 784-787. (1998).
3. Groen II, Baker CI. Scenes in the human brain: Comparing 2d versus 3d representations. *Neuron*. (2019).
4. Georgieva S, Peeters R, Kolster H, Todd JT, Orban GA. The processing of three-dimensional shape from disparity in the human brain. *Journal of Neuroscience*. (2009).
5. Linton P. Minimal theory of 3D vision: new approach to visual scale and visual shape. *Philosophical Transactions of the Royal Society B*. (2023).
6. Tong, F. Primary visual cortex and visual awareness. *Nature Reviews Neuroscience*, 4(3), 219-229. (2003).
7. Kim, I., Hong, S. W., Shevell, S. K., Shim, W. M. Neural representations of perceptual color experience in the human ventral visual pathway. *PNAS*, 117(23), 13145-13150. (2020).
8. Popham SF, Huth AG, Bilenko NY, Deniz F, Gao JS, Nunez-Elizalde AO, Gallant JL. Visual and linguistic semantic representations are aligned at the border of human visual cortex. *Nature neuroscience*. 24(11), 1628-36. (2021).
9. Ekman M, Kusch S, de Lange FP. Successor-like representation guides the prediction of future events in human visual cortex and hippocampus. *elife*. (2023).
10. Costa, J., Villa, C., Verhoeckx, K., Cirkovic-Velickovic, T., Schrama, D., Roncada, P., ... Holzhauser, T. Are

physicochemical properties shaping the allergenic potency of animal allergens?. *Clinical Reviews in Allergy Immunology*, 62(1), 1-36. (2022).

11. Chen, X., Rechavi, O. Plant and animal small RNA communications between cells and organisms. *Nature Reviews Molecular Cell Biology*, 23(3), 185-203. (2022).
12. Desquesnes, M., Gonzatti, M., Sazmand, A., Thévenon, S., Bossard, G., Boulangé, A., ... Berthier, D. A review on the diagnosis of animal trypanosomoses. *Parasites Vectors*, 15(1), 64. (2022).
13. Singh, I., Joseph, P., Heerdt, P. M., Cullinan, M., Lutchmansingh, D. D., Gulati, M., ... Waxman, A. B. Persistent exertional intolerance after COVID-19: insights from invasive cardiopulmonary exercise testing. *Chest*, 161(1), 54-63. (2022).
14. Risom, T., Glass, D. R., Averbukh, I., Liu, C. C., Baranski, A., Kagel, A., ... Angelo, M. Transition to invasive breast cancer is associated with progressive changes in the structure and composition of tumor stroma. *Cell*, 185(2), 299-310. (2022).
15. Rai, J., Kaushik, K. Reduction of animal sacrifice in biomedical science & research through alternative design of animal experiments. *Saudi Pharmaceutical Journal*, 26(6), 896-902. (2018).
16. Ferdowsian, H. R., Beck, N. Ethical and scientific considerations regarding animal testing and research. *PLoS one*, 6(9), e24059. (2011).
17. Díaz, L., Zambrano, E., Flores, M. E., Contreras, M., Crispín, J. C., Alemán, G., ... Bobadilla, N. A. Ethical considerations in animal research: the principle of 3R's. *Revista de investigacion clinica*, 73(4), 199-209. (2021).
18. Jansen, K., Casellas, C. P., Groenink, L., Wever, K. E., Masereeuw, R. Humans are animals, but are animals human enough? A systematic review and meta-analysis on interspecies differences in renal drug clearance. *Drug Discovery Today*, 25(4), 706-717. (2020).
19. Khaligh-Razavi, Seyed-Mahdi, and Nikolaus Kriegeskorte. Deep supervised, but not unsupervised, models may explain IT cortical representation. *PLoS Computational Biology*, e1003915. (2014).
20. Achterberg, J., Akarca, D., Strouse, D. J., Duncan, J., Astle, D. E. Spatially embedded recurrent neural networks reveal widespread links between structural and functional neuroscience findings. *Nature Machine Intelligence*, 5(12), 1369-1381. (2023).
21. LeCun, Yann, Bengio, Yoshua, and Hinton, Geoffrey. Deep learning. *Nature*, 521(7553). (2015).
22. Storrs KR, Kietzmann TC, Walther A, Mehrer J, Kriegeskorte N. Diverse deep neural networks all predict human inferior temporal cortex well, after training and fitting. *Journal of cognitive neuroscience*, 33(10):2044-64. (2021).
23. Kubilius J, Schrimpf M, Kar K, Rajalingham R, Hong H, Majaj N, Issa E, Bashivan P, Prescott-Roy J, Schmidt K, Nayebi A. Brain-like object recognition with high-performing shallow recurrent ANNs. *Advances in neural information processing systems*, 32. (2019).
24. Sexton NJ, Love BC. Reassessing hierarchical correspondences between brain and deep networks through direct interface. *Science advances*. (2022).
25. Baek S, Song M, Jang J, Kim G, Paik SB. Face detection in untrained deep neural networks. *Nature communications*, 12(1):7328. (2021).
26. Li W, Li J, Chu C, Cao D, Shi W, Zhang Y, Jiang T. Common Sequential Organization of Face Processing in the Human Brain and Convolutional Neural Networks. *Neuroscience*. (2024).
27. Palazzo S, Rundo F, Battiatto S, Giordano D, Spampinato C. Visual saliency detection guided by neural signals. *In2020 15th IEEE International Conference on Automatic Face and Gesture Recognition*. (2020).
28. Frey M, Doeller CF, Barry C. Probing neural representations of scene perception in a hippocampally dependent task using artificial neural networks. *CVPR*, (2023).
29. Bracci S, Mraz J, Zeman A, Leys G, Op de Beeck H. The representational hierarchy in human and artificial visual systems in the presence of object-scene regularities. *PLoS computational biology*. (2023).
30. Naselaris, T., Kay, K. N., Nishimoto, S., Gallant, J. L. Encoding and decoding in fMRI. *Neuroimage*, 56(2), 400-410. (2011).
31. Kamitani, Y., Tong, F. Decoding the visual and subjective contents of the human brain. *Nature neuroscience*, 8(5), 679-685. (2005).
32. Haxby, J. V., Gobbini, M. I., Furey, M. L., Ishai, A., Schouten, J. L., Pietrini, P. Distributed and overlapping representations of faces and objects in ventral temporal cortex. *Science*, 293(5539), 2425-2430. (2001).
33. Haynes, J. D., Rees, G. Predicting the orientation of invisible stimuli from activity in human primary visual cortex. *Nature neuroscience*, 8(5), 686-691. (2005).
34. Horikawa, T., Kamitani, Y. Generic decoding of seen and imagined objects using hierarchical visual features. *Nature communications*, 8(1), 15037. (2017).
35. Wen, H., Shi, J., Zhang, Y., Lu, K. H., Cao, J., Liu, Z. Neural encoding and decoding with deep learning for dynamic natural vision. *Cerebral cortex*, 28(12), 4136-4160. (2018).
36. Belyi, R., Gaziv, G., Hoogi, A., Strappini, F., Golan, T., Irani, M. From voxels to pixels and back: Self-supervision in natural-image reconstruction from fmri. *Advances in Neural Information Processing Systems*, 32. (2019).

37. Seeliger, K., Güçlü, U., Ambrogioni, L., Güçlütürk, Y., Van Gerven, M. A. Generative adversarial networks for reconstructing natural images from brain activity. *NeuroImage*, 181, 775-785. (2018).

38. Shen, G., Horikawa, T., Majima, K., Kamitani, Y. Deep image reconstruction from human brain activity. *PLoS computational biology*, 15(1), e1006633. (2019).

39. Chen, Z., Qing, J., Xiang, T., Yue, W. L., Zhou, J. H. Seeing beyond the brain: Conditional diffusion model with sparse masked modeling for vision decoding. *CVPR*. (2023).

40. Scotti, P., Banerjee, A., Goode, J., Shabalin, S., Nguyen, A., Dempster, A., ... Abraham, T. (2024). Reconstructing the mind's eye: fMRI-to-image with contrastive learning and diffusion priors. *Advances in Neural Information Processing Systems*, 36.

41. Allen, E. J., St-Yves, G., Wu, Y., Breedlove, J. L., Prince, J. S., Dowdle, L. T., ... Kay, K. A massive 7T fMRI dataset to bridge cognitive neuroscience and artificial intelligence. *Nature neuroscience*, 25(1), 116-126. (2022).

42. Ho, J., Jain, A., Abbeel, P. Denoising diffusion probabilistic models. *NeurIPS*, 33, 6840-6851 (2020).

43. Rombach, R., Blattmann, A., Lorenz, D., Esser, P., Ommer, B. High-resolution image synthesis with latent diffusion models. *CVPR*, 10684-10695 (2022).

44. Saharia, C., Chan, W., Saxena, S., Li, L., Whang, J., Denton, E. L., ... Norouzi, M. Photorealistic text-to-image diffusion models with deep language understanding. *NeurIPS*, 35, 36479-36494 (2022).

45. Poole, B., Jain, A., Barron, J., Mildenhall, B. DreamFusion: Text-to-3D using 2D Diffusion. *ICLR*, (2023).

46. Ben Mildenhall, Pratul P. Srinivasan, Matthew Tancik, Jonathan T. Barron, Ravi Ramamoorthi, Ren Ng. NeRF: Representing Scenes as Neural Radiance Fields for View Synthesis. *ECCV*, (2020).

47. Scotti, P. S., Banerjee, A., Goode, J., Shabalin, S., Nguyen, A., Cohen, E., ... Abraham, T. M. Reconstructing the Mind's Eye: fMRI-to-Image with Contrastive Learning and Diffusion Priors. *Advances in Neural Information Processing Systems*. (2024).

48. Szegedy, C., Vanhoucke, V., Ioffe, S., Shlens, J., Wojna, Z. Rethinking the inception architecture for computer vision. *CVPR*, 2818-2826 (2016).

49. Radford, A., Kim, J. W., Hallacy, C., Ramesh, A., Goh, G., Agarwal, S., ... Sutskever, I. Learning transferable visual models from natural language supervision. *ICML*, 8748-8763. (2021).

50. Tan, M., Le, Q. Efficientnet: Rethinking model scaling for convolutional neural networks. *ICML*, 6105-6114. (2019).

51. Caron, M., Misra, I., Mairal, J., Goyal, P., Bojanowski, P., Joulin, A. Unsupervised learning of visual features by contrasting cluster assignments. *NeurIPS*, 33, 9912-9924. (2020).

52. Welchman, A. E. The human brain in depth: how we see in 3D. *Annual review of vision science*, 2, 345-376 (2016).

53. Spring, A., Deutsch, G. Left brain right brain (p. 192). San Francisco: WH Freeman. (1981).

54. Corballis, M. C. Left brain, right brain: facts and fantasies. *PLoS biology*, 12(1), e1001767. (2014).

55. Iaccino, J. F. Left brain-right brain differences: Inquiries, evidence, and new approaches. *Psychology Press*. (2014).

56. Sun, T., Walsh, C. A. Molecular approaches to brain asymmetry and handedness. *Nature Reviews Neuroscience*, 7(8), 655-662. (2006).

57. Milner, D., Goodale, M. The visual brain in action. OUP Oxford (2006).

58. Squire, L. R., Stark, C. E., Clark, R. E. The medial temporal lobe. *Neuroscience*, 27, 279-306 (2004).

59. Squire, L. R., Zola-Morgan, S. The medial temporal lobe memory system. *Science*, 253(5026), 1380-1386 (1991).

60. Eichenbaum, H., Yonelinas, A. P., Ranganath, C. The medial temporal lobe and recognition memory. *Neuroscience*, 30, 123-152 (2007).

61. Sabatini, U., Boulanouar, K., Fabre, N., Martin, F., Carel, C., Colonnese, C., ... Rascol, O. Cortical motor reorganization in akinetic patients with Parkinson's disease: a functional MRI study. *Brain*, 123.2, 394-403 (2000).

62. Finn, Emily S., Russell A. Poldrack, James M. Shine. Functional neuroimaging as a catalyst for integrated neuroscience. *Nature*, 623(7986), 263-273 (2023).

63. Dresel, C., Haslinger, B., Castrop, F., Wohlschlaeger, A. M., Ceballos-Baumann, A. O. Silent event-related fMRI reveals deficient motor and enhanced somatosensory activation in orofacial dystonia. *Brain*, 129(1), 36-46 (2006).

64. Blood, A. J., Flaherty, A. W., Choi, J. K., Hochberg, F. H., Greve, D. N., Bonmassar, G., ... Jenkins, B. G. Basal ganglia activity remains elevated after movement in focal hand dystonia. *Annals of Neurology*, 55(5), 744-748 (2004).

65. Pujol, J., Roset-Llobet, J., Rosines-Cubells, D., Deus, J., Narberhaus, B., Valls-Sole, J., ... Pascual-Leone, A. Brain cortical activation during guitar-induced hand dystonia studied by functional MRI. *Neuroimage*, 12(3), 257-267 (2000).

66. Bucher, S. F., Seelos, K. C., Dodel, R. C., Reiser, M., Oertel, W. H. Activation mapping in essential tremor with functional magnetic resonance imaging. *Annals of Neurology*, 41(1), 32-40 (1997).

67. Dirkx, M. F., den Ouden, H., Aarts, E., Timmer, M., Bloem, B. R., Toni, I., Helmich, R. C. The cerebral network of Parkinson's tremor: an effective connectivity fMRI study. *Neuroscience*, 36(19), 5362-5372 (2016).

68. Aron, A. R., Schlaghecken, F., Fletcher, P. C., Bullmore, E. T., Eimer, M., Barker, R., ... Robbins, T. W. Inhibition of subliminally primed responses is mediated by the caudate and thalamus: evidence from functional MRI and Huntington's disease. *Brain*, 126(3), 713-723 (2003).

69. Hennenlotter, A., Schroeder, U., Erhard, P., Haslinger, B., Stahl, R., Weindl, A., ... Ceballos Baumann, A. O. Neural correlates associated with impaired disgust processing in presymptomatic Huntington's disease. *Brain*, 127(6), 1446-1453 (2004).

70. Zimbelman, J. L., Paulsen, J. S., Mikos, A., Reynolds, N. C., Hoffmann, R. G., Rao, S. M. fMRI detection of early neural dysfunction in preclinical Huntington's disease. *Journal of the International Neuropsychological Society*, 13(5), 758-769. (2007).

71. Playford, E. D., Jenkins, I. H., Passingham, R. E., Nutt, J., Frackowiak, R. S. J., Brooks, D. J. Impaired mesial frontal and putamen activation in Parkinson's disease: a positron emission tomography study. *Annals of Neurology*, 32(2), 151-161 (1992).

72. Jahanshahi, M., Jenkins, I. H., Brown, R. G., Marsden, C. D., Passingham, R. E., Brooks, D. J. Self-initiated versus externally triggered movements: I. An investigation using measurement of regional cerebral blood flow with PET and movement-related potentials in normal and Parkinson's disease subjects. *Brain*, 118(4), 913-933 (1995).

73. Catalan, M. J., Ishii, K., Honda, M., Samii, A., Hallett, M. A PET study of sequential finger movements of varying length in patients with Parkinson's disease. *Brain*, 122(3), 483-495 (1999).

74. Rascol, O., Sabatini, U., Fabre, N., Brefel, C., Loubinoux, I., Celsis, P., ... Chollet, F. The ipsilateral cerebellar hemisphere is overactive during hand movements in akinetic parkinsonian patients. *Brain*, 120(1), 103-110 (1997).

75. Shoham, A., Grosbard, I. D., Patashnik, O., Cohen-Or, D., Yovel, G. Using deep neural networks to disentangle visual and semantic information in human perception and memory. *Nature Human Behaviour*. (2024).

76. Enge, A., Süß, F., Rahman, R. A. Instant effects of semantic information on visual perception. *Journal of Neuroscience*. (2023).

77. McInnes, L., Healy, J., Melville, J. Umap: Uniform manifold approximation and projection for dimension reduction. Preprint at <https://arxiv.org/pdf/1802.03426.pdf> (2018).

78. Wang, J., Yang, Z., Hu, X., Li, L., Lin, K., Gan, Z., ... Wang, L. Git: A generative image-to-text transformer for vision and language. Preprint at <https://arxiv.org/pdf/2205.14100.pdf> (2022).

79. Liu, R., Wu, R., Van Hoorick, B., Tokmakov, P., Zakharov, S., Vondrick, C. Zero-1-to-3: Zero-shot one image to 3d object. *ICCV*, 9298-9309 (2023).

80. Ramesh, A., Dhariwal, P., Nichol, A., Chu, C., Chen, M. Hierarchical text-conditional image generation with clip latents. Preprint at <https://arxiv.org/pdf/2204.06125.pdf> (2022).

81. Xu, X., Wang, Z., Zhang, G., Wang, K., Shi, H. Versatile diffusion: Text, images and variations all in one diffusion model. *ICCV*, 7754-7765 (2023).

82. Shen, T., Gao, J., Yin, K., Liu, M. Y., Fidler, S. Deep marching tetrahedra: a hybrid representation for high-resolution 3d shape synthesis. *NeurIPS*, 34, 6087-6101 (2021).

83. Hoppe, H., DeRose, T., Duchamp, T., McDonald, J., Stuetzle, W. Mesh optimization. *SIGGRAPH*, 19-26 (1993).

84. Zhang, L., Rao, A., Agrawala, M. Adding conditional control to text-to-image diffusion models. *ICCV*, 3836-3847 (2023).

85. Zhang, H., Cisse, M., Dauphin, Y. N., Lopez-Paz, D. mixup: Beyond empirical risk minimization. *ICLR*. (2018).

86. Radford, A., Kim, J. W., Hallacy, C., Ramesh, A., Goh, G., Agarwal, S., ... Sutskever, I. Learning transferable visual models from natural language supervision. *ICML*, 8748-8763. (2021).

87. Hinton, G., Vinyals, O., Dean, J. Distilling the Knowledge in a Neural Network. *stat*, 1050, 9. (2015).

88. Lin, T. Y., Maire, M., Belongie, S., Hays, J., Perona, P., Ramanan, D., ... Zitnick, C. L. Microsoft coco: Common objects in context. *ECCV*, Part V 13, 740-755. (2014).

89. Welvaert, Marijke, and Yves Rosseel. A review of fMRI simulation studies. *PloS one*, e101953 (2014).

90. Potetz, B., Lee, T. S. Statistical correlations between two-dimensional images and three-dimensional structures in natural scenes. *JOSA A*. (2003).

91. He, Y., Bai, Y., Lin, M., Zhao, W., Hu, Y., Sheng, J., ... Liu, Y. J. T³ Bench: Benchmarking Current Progress in Text-to-3D Generation. Preprint at <https://arxiv.org/abs/2310.02977> (2023).

92. Haselton, M. G., Nettle, D., Andrews, P. W. The evolution of cognitive bias. *The handbook of evolutionary psychology*, 724-746 (2015).

93. Johnson, C. A., Casson, E. J. Effects of luminance, contrast, and blur on visual acuity. *Optometry and vision science*, 72, 864-869 (1995).

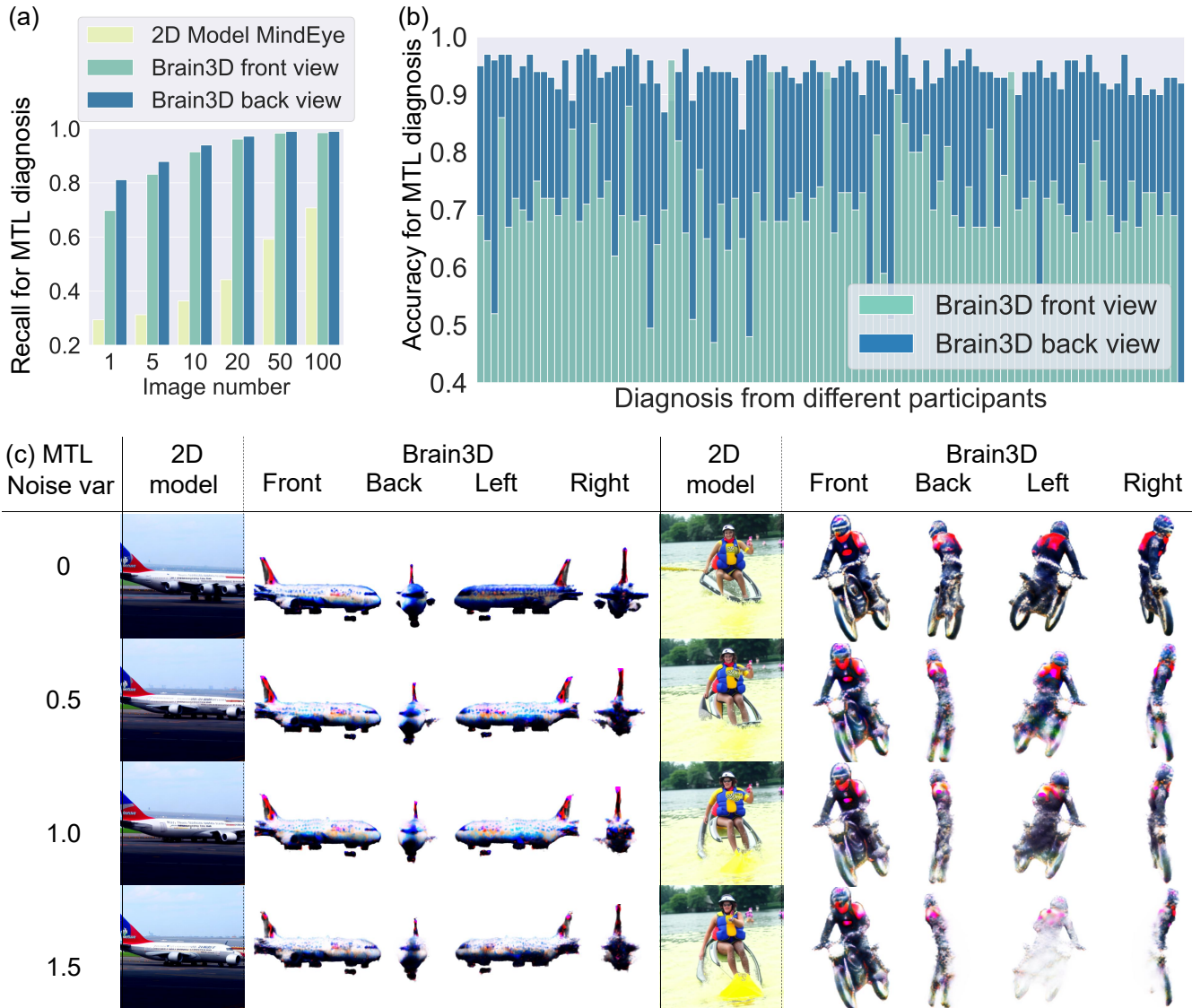


Figure s1. 3D visualization capability of Brain3D enhances discrimination of MTL disorders. (a) In scenarios with a limited number of testing images, the back view offered by Brain3D's 3D visualization achieves the highest F1 scores compared to the front view, much higher than the 2D model. This result indicates an enhanced diagnostic efficiency of Brain3D for identifying disorders in MTL. (b) Analysis shows that the back view consistently provides a more accurate diagnosis of MTL region disorders compared to the front view across all participants. (c) In cases of MTL region disorders, the back view reveals a greater degree of ambiguity compared to the front view, while in 2D model MindEye⁴⁷, MTL brain disorder does not exhibit any regular features and thus cannot be distinguished from disorders in other brain areas.

		V1	V2	V3	V4	MTL
		0.89	0.03	0.03	0.01	0.03
Disorder region	V1	0.13	0.34	0.29	0.21	0.09
	V2	0.12	0.24	0.35	0.28	0.06
	V3	0.09	0.18	0.30	0.39	0.07
	V4	0.02	0.03	0.02	0.04	0.87
	MTL	0.00	0.01	0.01	0.02	0.95

		V1	V2	V3	V4	MTL
		0.97	0.01	0.01	0.00	0.01
Disorder region	V1	0.10	0.34	0.30	0.25	0.06
	V2	0.09	0.25	0.39	0.26	0.03
	V3	0.06	0.19	0.33	0.39	0.05
	V4	0.00	0.01	0.01	0.02	0.95
	MTL	0.00	0.01	0.01	0.02	0.87

		V1	V2	V3	V4	MTL
		0.99	0.00	0.00	0.00	0.00
Disorder region	V1	0.07	0.42	0.30	0.21	0.03
	V2	0.06	0.23	0.45	0.27	0.01
	V3	0.04	0.15	0.37	0.43	0.02
	V4	0.00	0.00	0.01	0.01	0.98
	MTL	0.00	0.00	0.01	0.00	0.99

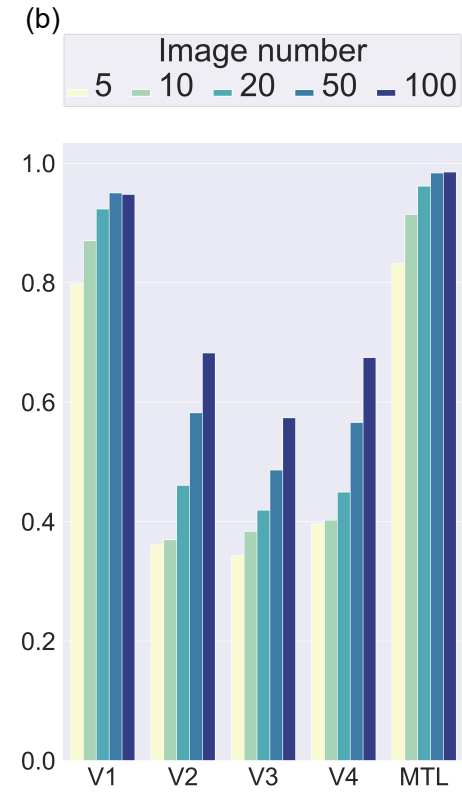


Figure s2. Advancing efficient diagnosis with limited images. (a) Our study further conducted experiments where participants were given restricted sets of visualizations to determine the feasibility of low-cost diagnosis. This approach underscores the remarkable diagnostic proficiency within the V1 and medial temporal lobe (MTL) regions, even when using a limited quantity of images. We present heatmaps that detail diagnostic accuracy, utilizing varying sets of images - namely, batches of 5, 10, 20, and 50 images per patient. The results demonstrate that participants could accurately discern disorders in the V1 and MTL regions, despite the limited number of images available. (b) Bar-plot presents the recall of V1, V2, V3, V4 and MTL region diagnosis under different image number. It suggests that reliable diagnostic conclusions of V1 and MTL can be drawn with fewer images, leading to a substantial reduction in time and resources required for diagnosis. This efficiency is especially critical in clinical settings, where swift and accurate diagnosis is paramount.

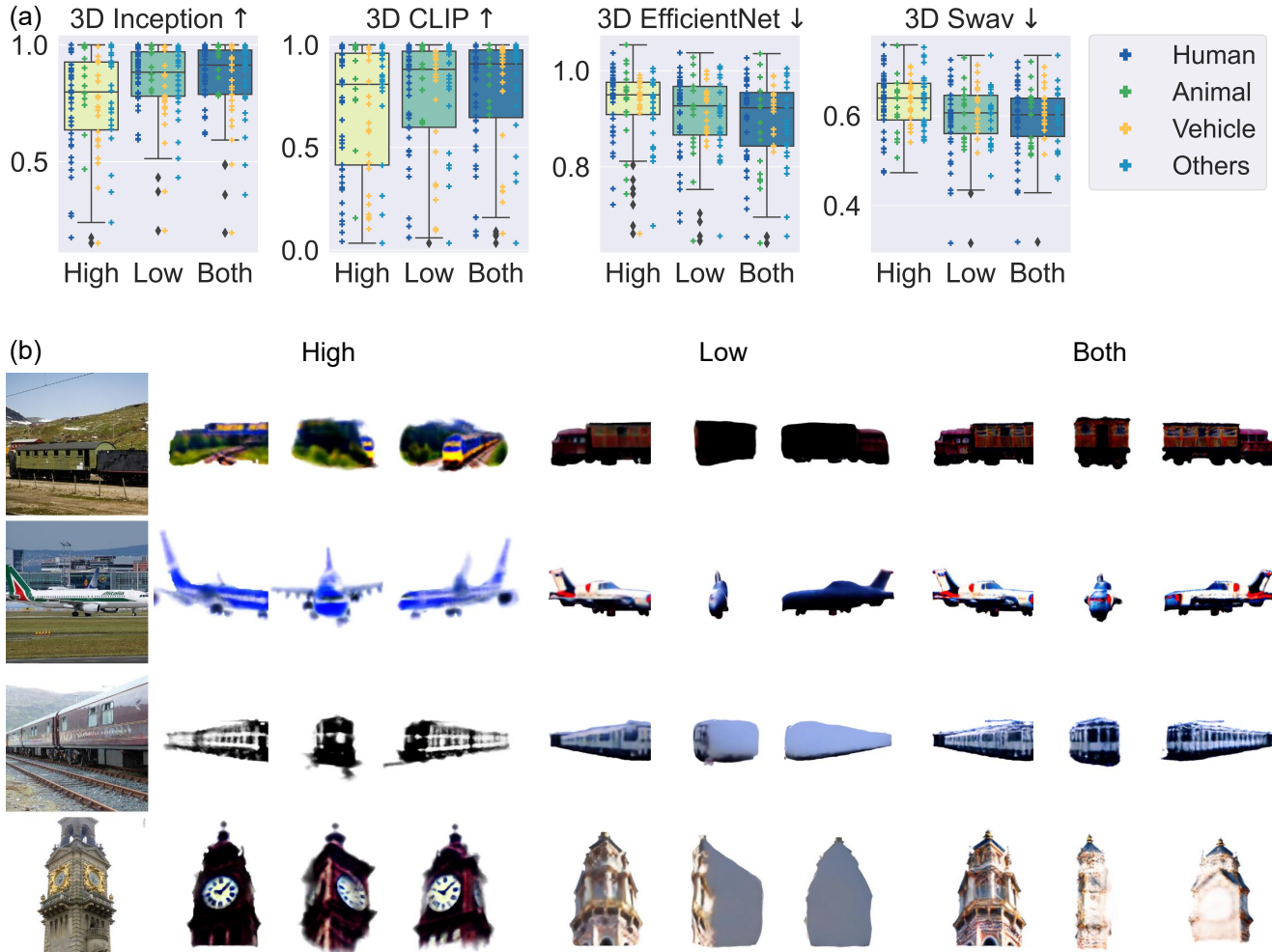


Figure s3. Low-level and high-level embeddings are both detrimental in visual processing. (a) Integration of both Low-Level and High-Level is beneficial for human brains to better perceive objects. Boxplots exhibit the median, the 25th, and 75th percentiles as box edges among the four metrics. Crosses (+) represent the scores of each image with the category displayed to participants. (b) High-level embedding in fMRI concentrates on abstract semantic information, while low-level embedding in fMRI focuses on color and texture information. The synergy of these two embeddings results in a more holistic perception of objects in the human brain, encapsulating both semantic depth and textural detail.

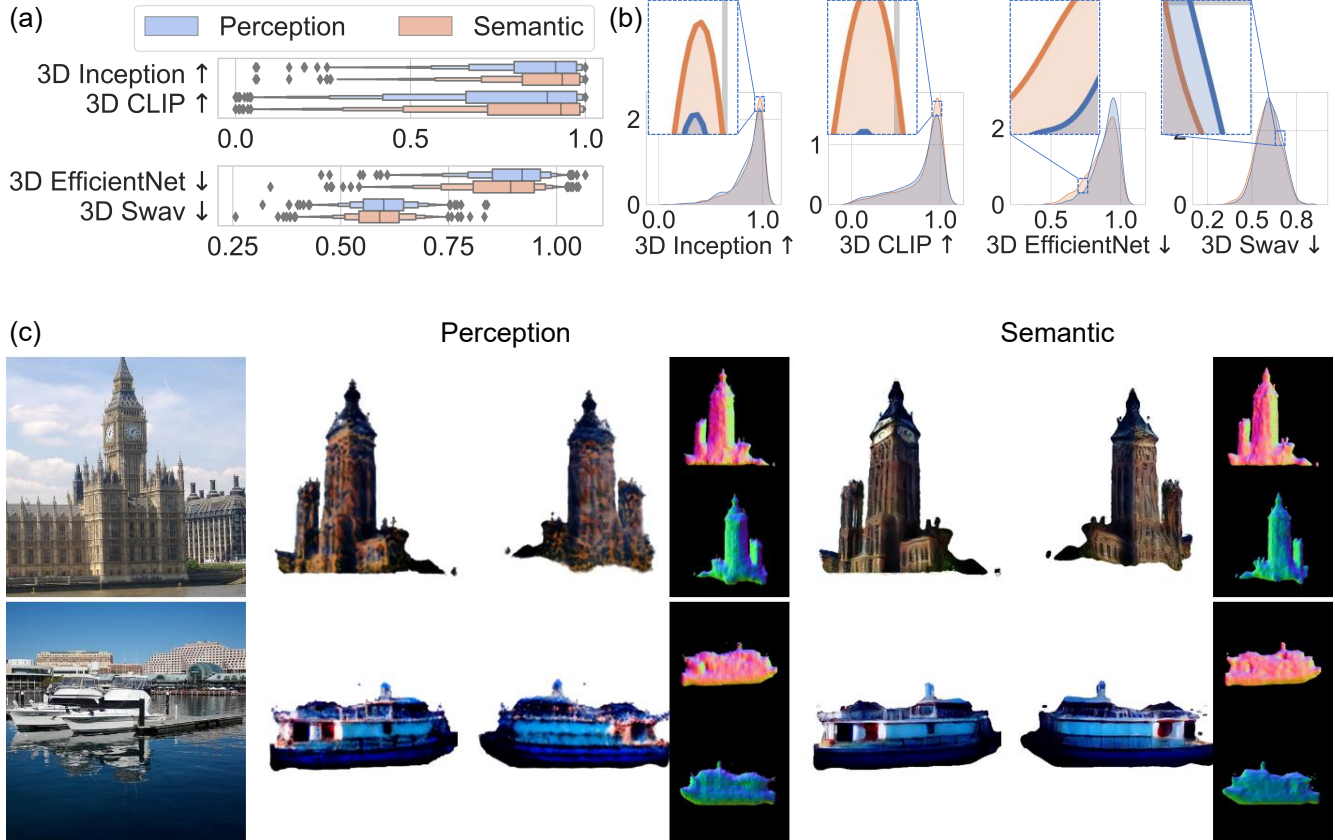


Figure s4. Enhanced generation quality through semantic stage and UMAP projection. (a) The semantic stage outperforms the perception stage in all evaluation metrics in every quantile. Boxen plot shows 5%, 15%, 25%, 50%, 75%, 85%, and 95% percentile. (b) During the semantic stage, there is a noticeable increase in the proportion of high 3D Inception and 3D CLIP scores, along with a leftward shift in the 3D EfficientNet and 3D Swav scores. This shift indicates a more refined and accurate generation of 3D objects. (c) 3D objects generated in the semantic stage exhibit a noticeably higher fidelity compared to those from the perception stage, showcasing the enhanced capabilities of the semantic processing. See Fig. s9 for more comparisons.

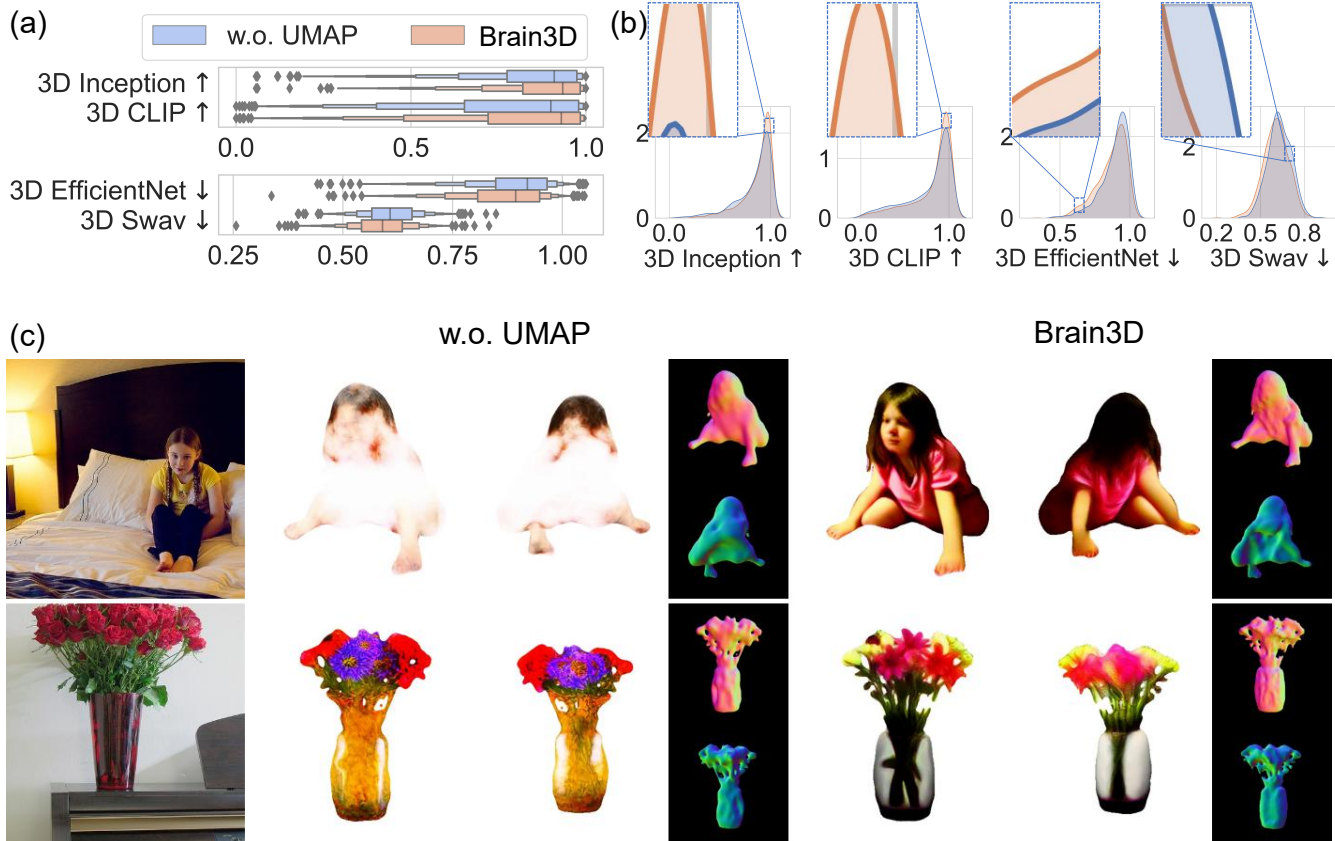


Figure s5. Enhanced generation quality through UMAP projection. (a) UMAP projection improves generation quality among all metrics in every quantile. (b) Utilizing UMAP projection not only achieves higher 3D Inception and 3D CLIP scores but also contributes to lower 3D EfficientNet and 3D Swav scores. This outcome demonstrates the projection's ability to refine and improve the overall quality. (c) The employment of UMAP projection significantly enhances textural stability in fMRI-generated content, pointing to its efficacy in producing more consistent and reliable outputs. See Fig. s10 for more comparisons.

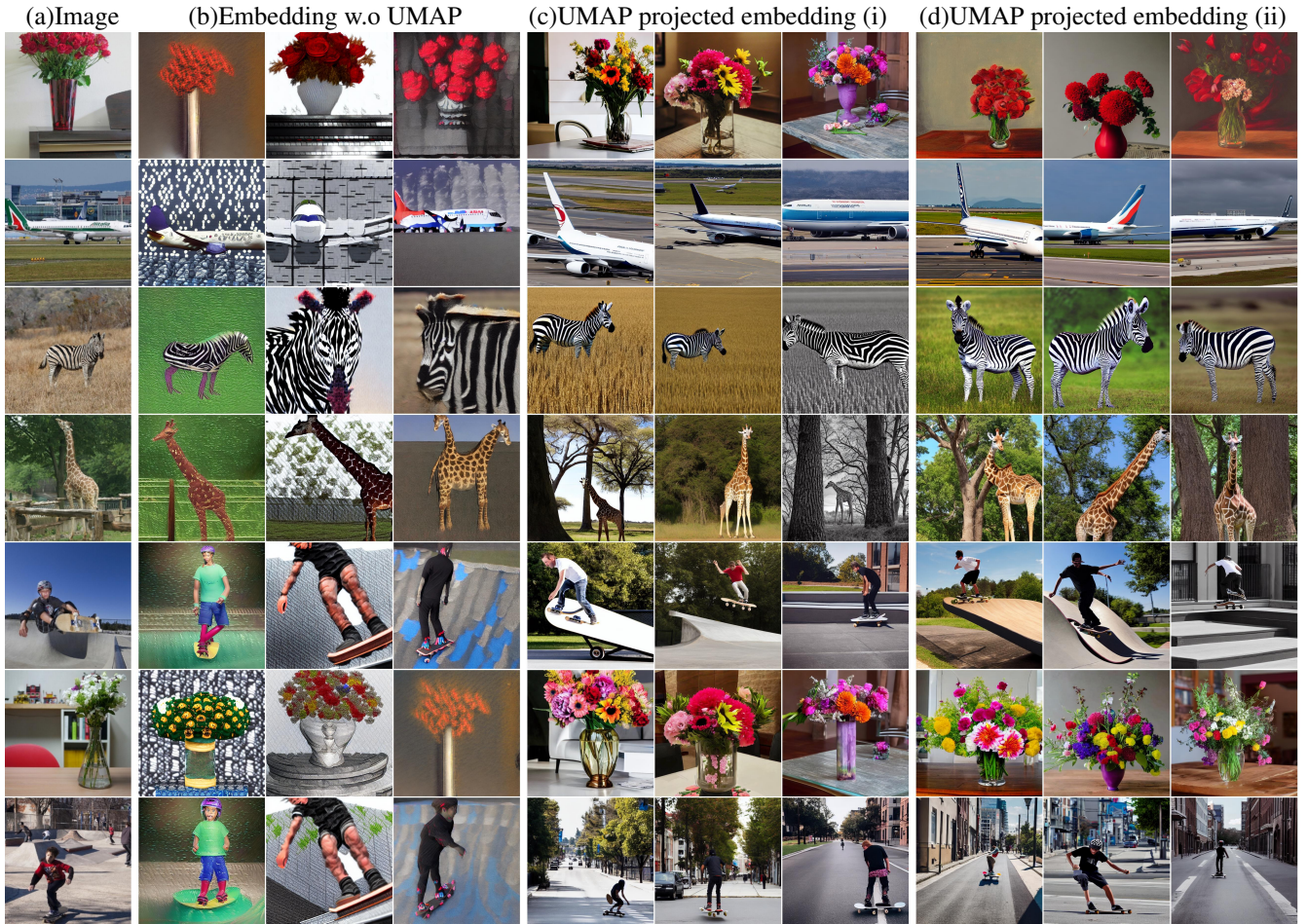


Figure s6. Variety in high-level information. (a) The reference images presented to the participants. (b) Images generated by Stable Diffusion⁴³ conditioned on the high-level embedding without UMAP⁷⁷ projection. (c, d) Images conditioned on different high-level embeddings after UMAP projection. It shows that the high-level embedding directly extracted from fMRI comes with high diversity and noise. Our UMAP projection can significantly mitigate this challenge.



Figure s7. More examples on evaluating the role of left and right hemispheres. With a specific image as stimulus, the left and right hemispheres differ in perception. In general, the left favors finer details and intricate structures, while the right focuses more on overall shape and silhouette. Their collaboration exhibits an improvement in 3D generation quality.



Figure s8. More examples on different vision regions. V1 region extracts and restores features and silhouettes of the given image, while V2, V3, and V4 concentrate on a fraction of texture details.

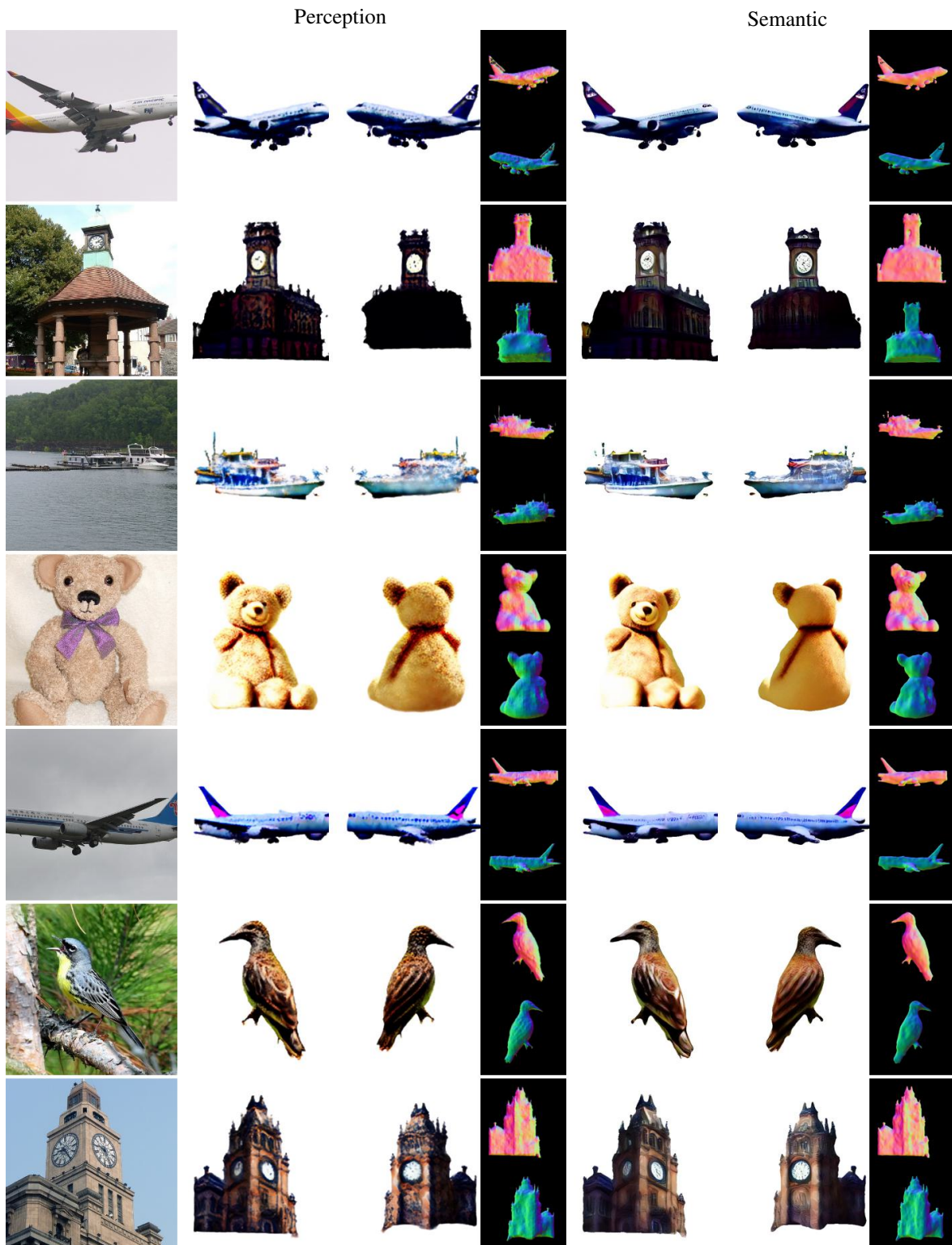


Figure s9. More examples on ablating the effect of semantic stage. The semantic stage 3D objects show higher fidelity than the perception stage.

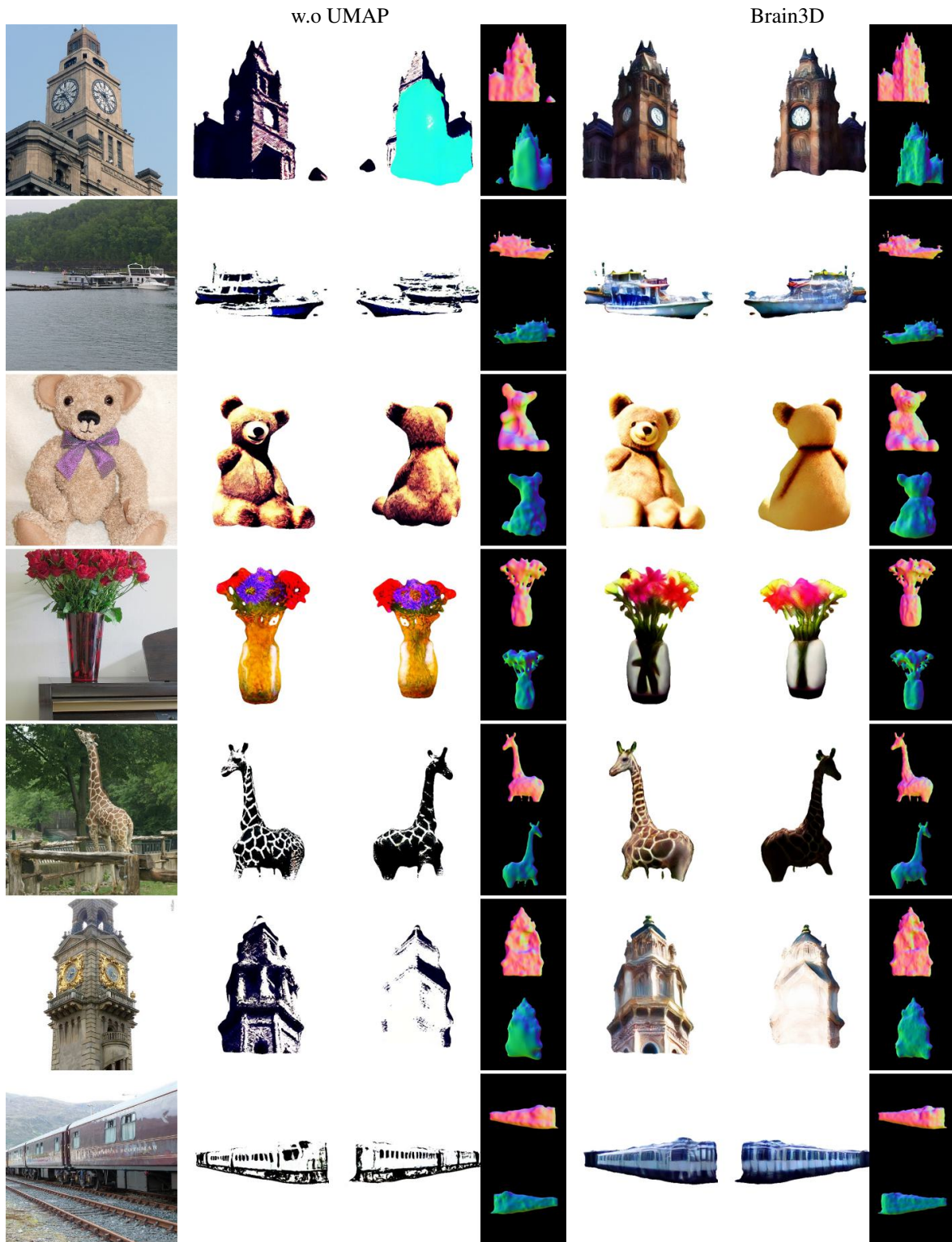


Figure s10. More examples on ablating the effect of UMAP projection. UMAP projection improves textural stability of view generation.